Abstract

The flow over an isolated two-dimensional mountain is investigated using a vertical slice version of the Met Office Unified model. The upstream flow is of constant wind speed U and constant Brunt-Väisälä frequency N. The dimensionless parameters for this problem are the Froude number $Fr = U/NH$, Rossby number $Ro = U/fL$ and the ratio f/N, where L is the half-width of the mountain, f is the Coriolis parameter and H is the maximum height of the mountain. The solution is approximately determined by Ro and Fr if H/L is fixed. It is found that the limit $f \to 0$ is singular (i.e. the flow solution does not converge to the $f = 0$ solution), and there exist multiple solutions; one for $f = 0$ and two obtained in the limits $f \to 0^+$ and $f \to 0^-$. A barrier jet on the upstream side of the mountain exists within the Rossby radius of deformation $L_R = NH/f$. The strength of the barrier jet increases linearly as both f and N increase at the same rate keeping f/N constant. Vertical kinetic energy is used as a measure of gravity wave activity. It is found that for $f > f_0/4$ vertical KE decreases as f increases. As Ro decreases, it is shown that there is second-order convergence to the semi-geostrophic solution. For $f > 0$ pressure drag on the mountain decreases as f increases. When both f and N are decreased together the drag does not vary by more than 20% from the mean value.

Contents

List of Symbols

D	Pa	pressure drag
f	s^{-1}	Coriolis parameter
g	ms^{-2}	acceleration due to gravity
H	m	vertical height scale
L	m	horizontal length scale
L_m	m	model upstream influence
L_R	m	Rossby radius of deformation
N	s^{-1}	Brunt-Väisälä frequency
p	Pa	pressure
$S_{f,N}$		scaling factor of f and N
t	s	time
U	ms^{-1}	horizontal speed scale
u, v, w	ms^{-1}	velocity components
x, y, z		Cartesian coordinates
$\mathbf{k}$		unit vector in z direction
$\mathbf{v}$	ms^{-1}	velocity vector
α		weighting parameter
θ	K	potential temperature
ρ	kgm^{-3}	density

List of Figures

List of Tables

Chapter 1

Introduction

The problem of stratified flow over mountains has been studied for several decades. A “classical” problem in this field of study is that of steady, Boussinesq, hydrostatic, nonrotating flow, unbounded above (Smith 1989).

There are a wide range of scales that must be considered, for example, the nature of a disturbance caused by a narrow hill is quite different to that of a broad plateau, even if the height of the terrain and other factors are the same. For small-scale mountains or hills which are $100m$ to $50km$ wide, the flow can be considered without including the Coriolis force. For mesoscale and synoptic-scale mountains (wider than $50km$) the rotation of the Earth cannot be neglected. Examples of such mountains include the Scandinavian mountain range (width $\sim 300km$), the Alps (width $\sim 250km$), and the Canadian Rockies (width $\sim 400km$) (Smith 1979b).

There are many features of airflow over mountains, both upstream and downstream of the mountain. A few examples include upstream blocking, barrier jets, gravity waves, trapped lee waves and föhn winds.

The blocking of low-level air is one of the most important ways in which mountains affect the air flow. The heavy surface air may have difficulty in running upslope and due to this, the surface level flow tends to slow as it approaches the mountain (Smith 1979a). In the nonrotating case this upstream layer of stagnant fluid will eventually be of infinite extent. However, in the rotating case the Coriolis force limits this extent to a maximum length on the order of the Rossby radius of deformation before receding back toward the mountain. Thus, the Coriolis force is the major factor which limits the strength and extent of the flow blocking (Pierrehumbert and Wyman 1985).

An effect of flow blocking is that it causes air at levels just above the mountain top to be forced down the lee-side of the mountain as a type of föhn (Shutts 1998). A föhn is a warm, dry wind that descends in the lee of a mountain range. 'Föhn' is the regional name for this type of wind in the European Alps. It has a different name in other regions, such as the 'chinook' of the Rocky Mountains, or the 'nor'wester' in New Zealand. Winds of this type are noted for their violence and gustiness. For example, on the eastern slopes of the Rocky Mountains wind speeds have reached in excess of $56ms^{-1}$ (Quaile 2001).

Many patterns of the flow over mountains are gravity waves, in which the vertical displacement from equilibrium is restored by gravity, with subsequent under- and overshooting of the equilibrium level giving rise to a series or train of waves (McIlveen 1997). Gravity waves can appear as vertical displacements of potential temperature contours which tilt upstream with height, indicating an upward transport of energy and a downward transport of momentum (Sprenger and Schär 2001). Another example of mountain waves are lee waves, which Pierrehumbert and Wyman (1985) describe as undular motions that, given sufficient time, extend arbitrarily far downstream of the mountain without diminution of amplitude.

In order to describe the flow problem, dimensionless parameters are used. By varying these, different regimes of flow can be investigated. There are many of these parameters to choose from but only a selection are used in this project. However, these still enable us to simulate a range of flow solutions. We now introduce three dimensionless parameters which are of importance here.

One important dimensionless parameter is the Rossby number, *Ro*. Here, we give a brief description of how this number is derived. The full horizontal momentum equation (introduced properly later in Section 2.1) can be written

$$\frac{D\mathbf{v}}{Dt} + f\mathbf{k} \times \mathbf{v} + \frac{1}{\rho}\nabla_H p = 0$$

where $\nabla_H = \left(\frac{\partial}{\partial x}, \frac{\partial}{\partial y}\right)$ and f is the Coriolis parameter. We perform scale analysis on this equation by using U = horizontal speed scale, L = horizontal length scale and L/U = time scale. Thus we can scale each term of the horizontal momentum equation as follows:

$$\textit{Term 1} \sim \frac{U^2}{L} \qquad \textit{Term 2} \sim fU \qquad \textit{Term 3} \sim \frac{\Delta p}{\rho L}.$$

If we compare the magnitudes of Terms 1 and 2 we obtain

$$\frac{\textit{Term 1}}{\textit{Term 2}} \sim \frac{U^2}{LfU} = \frac{U}{fL} \equiv Ro$$

and this is the Rossby number. The smallness of Ro is a measure of the validity of the geostrophic approximation, and the importance of the effect of rotation (Holton 1992). So for $Ro \ll 1$ the horizontal momentum equation can be approximated by neglecting Term 1 and the flow is called "geostrophic", which represents an exact balance between the pressure gradient and the Coriolis force.

Another dimensionless parameter of interest is the Froude number defined as

$$Fr = \frac{U}{NH} \tag{1.1}$$

where H is the height of the mountain and the Brunt-Väisälä frequency $N = \left(\frac{g}{\overline{\theta}} \frac{\partial \overline{\theta}}{\partial z}\right)^{\frac{1}{2}}$ where g is acceleration due to gravity and $\overline{\theta}$ is a reference potential temperature.. The Froude number is a measure of the importance of stratification. If $Fr \lesssim 1$ stratification effects are important, and the smaller Fr is, the more important these effects are. The stronger the stratification, the weaker the vertical velocity and vertical displacements (Cushman-Roisin 1994). Note that H is a depth scale, which could also have been chosen to be the total height of the domain or a height scale related to a shear in U. However, since U (as well as N) are constant with height in this project and the mountain is an appreciable height, mountain height is the depth scale chosen.

The ratio of Ro and Fr is NH/fL, or AN/f where A is the aspect ratio H/L. Thus, if A is held constant, a third important parameter is the ratio f/N.

Figure 1.1 indicates how the flow is influenced for different values of Ro and Fr.

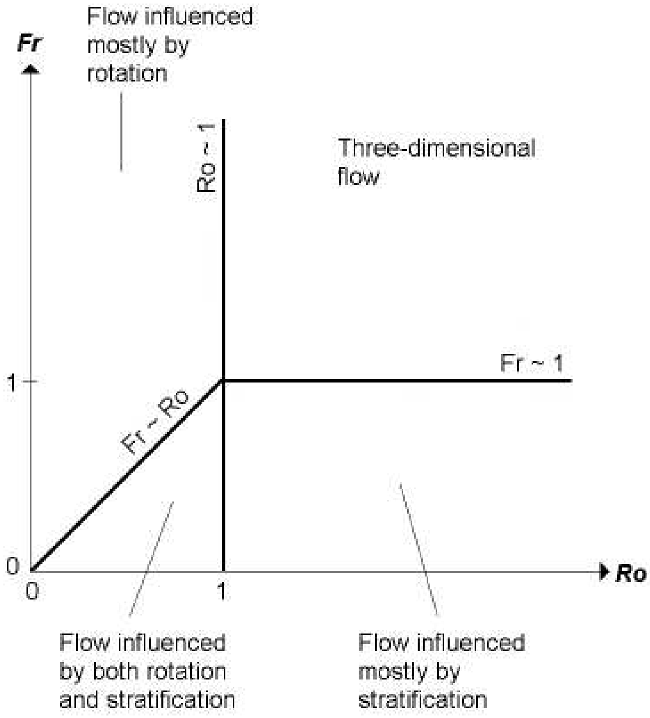

Figure 1.1: *Influence of rotation and stratification on the flow as a function of* Ro *and* Fr. *(Adapted from Cushman-Roisin (1994))*

The problem considered in this project is that of a flow of constant speed with height (U) and constant stratification with height (N). This flow goes over an isolated, two-dimensional cosine mountain of half-width L and maximum height H (Fig. 1.2).

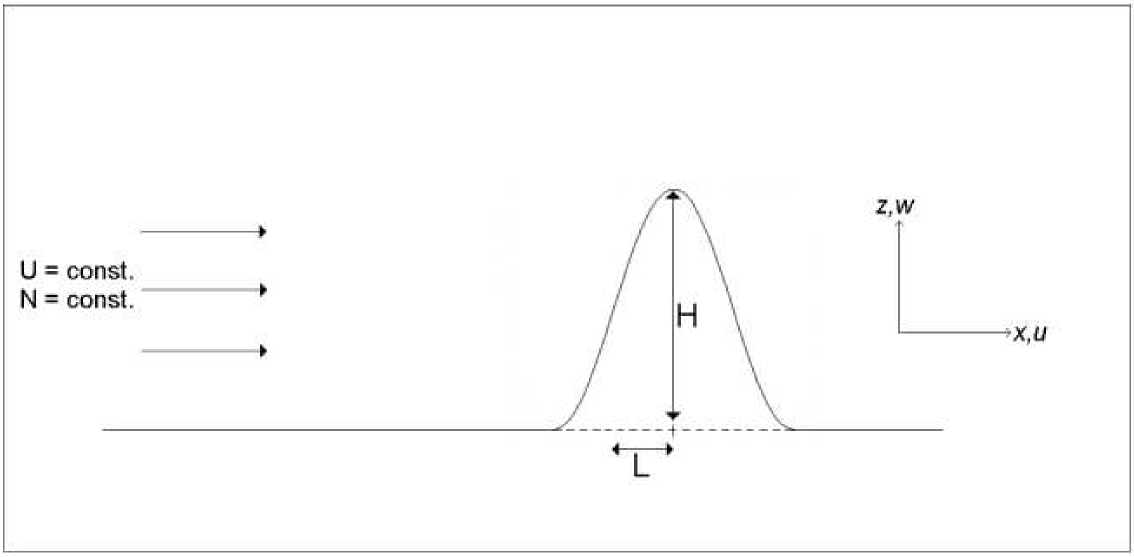

Figure 1.2: *Schematic of the flow problem considered in this project. The mountain is a cosine shape of half-width L and maximum height H. The upstream flow speed U and the stratification N are both constant with height.*

We can think of the mountain as a ridge which extends infinitely far in the y direction. This is 'frontal scaling' in which one dimension is infinitely larger than the other and thus the use of semi-geostrophic theory is appropriate in this project. Cullen (2000) states that semi-geostrophic theory is second-order accurate (or better) if one horizontal length-scale is larger than the Rossby radius of deformation or if the ratio of horizontal to vertical scales is is greater than f/N, while it is asymptotically valid (first-order accurate) for all small Ro cases.

The methodology and results of this project are set out as follows. In Chapter 2 we introduce the full Euler equations which are the ones solved by the model used in this project. In order to analyse their solutions we first simplify these equations by using the Boussinesq and anelastic approximations. We then non-dimensionalise and linearise these basic equations and solve them to obtain non-trivial solutions which describe different regimes of flow.

In Chapter 3 we present a brief overview of the model being used, which is a vertical slice version of the Met Office Unified model. A more comprehensive description of this model is given by Cullen *et al.* (1997). Experiments are then conducted to find the choice of CFL number and weighting parameter α which give the fastest convergence to steady state (Section 3.2). Experiments are also conducted to find the steady state solutions as f varies, and steady states as U varies.

An aim of this project is to explore regimes where rotation is important. In Chapter 4 we begin by examining the singularity of the limit $f \to 0$ and we indeed expect it to be singular in accordance with experiments conducted by Sprenger and Schär (2001). The demonstration of this singularity is another aim of the project. We then see how the upstream influence varies with f. We expect that as f decreases upstream influence increases. Cullen *et al.* (1987) found that in the absence of rotation there is no limit on the upstream influence, but if rotation is present this distance is restricted. The variation of vertical kinetic energy and pressure drag with f is also investigated since vertical KE is a useful measure of gravity wave activity.

In Chapter 5 we investigate the importance of the strength of the upstream flow speed. Since both Ro and Fr depend on U they will vary at the same rate. Another of our aims is to show that the limit solution for small Ro and Fr shall be semi-geostrophic and in this chapter we investigate the convergence to this solution. The semi-geostrophic solution is very singular so validating its limit is non-trivial. An aim of the project is to demonstrate the expected sensitivity of the semi-geostrophic limit to Ro and Fr. From Sprenger and Schär (2001) we expect the amplitude of vertical displacements to decrease as U decreases.

In Chapter 6 we see how both rotation and stratification effect the flow solution in the form of the dimensionless parameter f/N, which is kept constant in each of the experiments. We will demonstrate how well the flow is determined by Ro and Fr by achieving the same values as in Chapter 5 by varying f and N instead of U. We expect to show that the solution is accurately determined if it is in a linear regime (as we discuss in Chapter 2).

Finally, in Chapter 7 we discuss the main conclusions drawn from this project.

Chapter 2

Linear Analysis of the Basic Equations

2.1 Linearisation of the basic equations

We must begin by introducing the full Euler equations

$$\frac{Du}{Dt}+\frac{1}{\rho}\frac{\partial p}{\partial x}-fv=0 \tag{2.1}$$

$$\frac{Dv}{Dt}+\frac{1}{\rho}\frac{\partial p}{\partial y}+fu=0 \tag{2.2}$$

$$\frac{Dw}{Dt}+\frac{1}{\rho}\frac{\partial p}{\partial z}+g=0 \tag{2.3}$$

$$\frac{D\theta}{Dt}=0 \tag{2.4}$$

$$\frac{D\rho}{Dt}+\rho\nabla.\mathbf{u}=0 \tag{2.5}$$

where $\frac{D}{Dt}=\frac{\partial}{\partial t}+u\frac{\partial}{\partial x}+v\frac{\partial}{\partial y}+w\frac{\partial}{\partial z}$, ρ is density (kgm^{-3}), g is acceleration due to gravity (ms^{-2}) and θ is potential temperature (K). Equations (2.1) and (2.2) are the horizontal momentum equations, (2.3) is the vertical momentum equation, (2.4) is the thermodynamic equation and (2.5) is the mass conservation equation. These are the equations that are being solved by the model used in this project.

For the purposes of understanding the solution some approximations are now made, including the Boussinesq and anelastic approximations, in order to reduce the above equations to a simpler form. In the Boussinesq approximation density is replaced by a constant mean value, ρ_{ref}, everywhere except in the buoyancy term in the vertical momentum equation (Holton 1992), and the anelastic approximation is made such that $\nabla.(\rho_{\mathrm{ref}}\mathbf{u}) = 0$. Also, a reference state is subtracted with uniform θ_0.

If, for these purposes, we assume that $\rho \approx 1kgm^{-3}$ the basic, anelastic, incompressible $(\frac{D\rho}{Dt} = 0)$ Boussinesq equations are

$$p^* = \rho RT \tag{2.6}$$

$$\frac{\partial u^*}{\partial t^*} + u^*\frac{\partial u^*}{\partial x^*} + v^*\frac{\partial u^*}{\partial y^*} + w^*\frac{\partial u^*}{\partial z^*} + \frac{\partial p^*}{\partial x^*} - fv^* = 0 \tag{2.7}$$

$$\frac{\partial v^*}{\partial t^*} + u^*\frac{\partial v^*}{\partial x^*} + v^*\frac{\partial v^*}{\partial y^*} + w^*\frac{\partial v^*}{\partial z^*} + \frac{\partial p^*}{\partial y^*} + fu^* = 0 \tag{2.8}$$

$$\frac{\partial w^*}{\partial t^*} + u^*\frac{\partial w^*}{\partial x^*} + v^*\frac{\partial w^*}{\partial y^*} + w^*\frac{\partial w^*}{\partial z^*} + \frac{\partial p^*}{\partial z^*} - \frac{g^*\theta_1}{\theta_0} = 0 \tag{2.9}$$

$$\frac{\partial \theta^*}{\partial t^*} + u^*\frac{\partial \theta^*}{\partial x^*} + v^*\frac{\partial \theta^*}{\partial y^*} + w^*\frac{\partial \theta^*}{\partial z^*} = 0 \tag{2.10}$$

$$\frac{\partial u^*}{\partial x^*} + \frac{\partial v^*}{\partial y^*} + \frac{\partial w^*}{\partial z^*} = 0 \tag{2.11}$$

where (2.6) is the equation of state for dry air ($R = 287Jkg^{-1}K^{-1}$ is the gas constant for dry air), (2.7) and (2.8) are the horizontal momentum equations, (2.9) is the vertical momentum equation, (2.10) is the thermodynamic equation and (2.11) is the mass conservation equation. The '$*$' indicates that the equations are dimensional.

We now non-dimensionalise Eqs. (2.7) - (2.11) by using scalings of the form

$$
\begin{aligned}
u^* &= Uu \\
v^* &= Uv \\
w^* &= Ww \\
t^* &= Tt \\
x^* &= Lx \\
y^* &= Ly \\
z^* &= Hz \\
\theta_1 &= \theta_0\theta \\
p^* &= Pp
\end{aligned}
$$

and we choose $U = LT^{-1}$, $W = HT^{-1}$ and $P = L^2T^{-2}$.

By using the above scalings and multiplying through by T/U, the non-dimensional horizontal momentum equations become

$$\frac{\partial u}{\partial t} + u\frac{\partial u}{\partial x} + v\frac{\partial u}{\partial y} + w\frac{\partial u}{\partial z} + \frac{\partial p}{\partial x} - Ro^{-1}v = 0 \tag{2.12}$$

$$\frac{\partial v}{\partial t} + u\frac{\partial v}{\partial x} + v\frac{\partial v}{\partial y} + w\frac{\partial v}{\partial z} + \frac{\partial p}{\partial y} + Ro^{-1}u = 0 \tag{2.13}$$

and we see that the dimensionless Rossby number is now present as a control parameter. Doing the same as above but this time multiplying through by T/W, the non-dimensional vertical momentum equation becomes

$$\frac{\partial w}{\partial t} + u\frac{\partial w}{\partial x} + v\frac{\partial w}{\partial y} + w\frac{\partial w}{\partial z} + A^{-2}\frac{\partial p}{\partial z} - g\theta = 0 \tag{2.14}$$

where the aspect ratio $A = H/L$, and dimensionless $g = g^*T^2/H$. Trivially, the non-dimensional thermodynamic and continuity equations are

$$\frac{\partial \theta}{\partial t} + u\frac{\partial \theta}{\partial x} + v\frac{\partial \theta}{\partial y} + w\frac{\partial \theta}{\partial z} = 0 \tag{2.15}$$

and

$$\frac{\partial u}{\partial x} + \frac{\partial v}{\partial y} + \frac{\partial w}{\partial z} = 0. \tag{2.16}$$

We now define the linearised, non-dimensional form of the Boussinesq hydrostatic balance approximation to be

$$A^{-2}\frac{\partial \overline{p}}{\partial z} = g\overline{\theta}. \tag{2.17}$$

We linearise about a state of rest ($p = \overline{p}(z)$, $\theta = \overline{\theta}(z)$) and divide the dependant variables into constant basic state portions (denoted by overbars) and perturbation portions (denoted by primes), i.e.

$$\begin{aligned} u &= u' \\ v &= v' \\ w &= w' \\ p &= \overline{p}(z) + p' \\ \theta &= \overline{\theta}(z) + \theta'. \end{aligned}$$

Substituting for u, v, w and p in (2.7) and (2.8), and cancelling products of perturbation terms (because we assume these to be small compared to the dominant terms) gives the linearised horizontal momentum equations

$$\frac{\partial u'}{\partial t} + \frac{\partial p'}{\partial x} - Ro^{-1}v' = 0 \tag{2.18}$$

$$\frac{\partial v'}{\partial t} + \frac{\partial p'}{\partial y} + Ro^{-1}u' = 0. \tag{2.19}$$

Doing the same for (2.9) but also substituting for θ gives

$$\frac{\partial w'}{\partial t} + A^{-2}\left(\frac{\partial \overline{p}}{\partial z} + \frac{\partial p'}{\partial z}\right) - g\overline{\theta} - g\theta' = 0,$$

and by using (2.17) we obtain the linearised vertical momentum equation

$$\frac{\partial w'}{\partial t} + A^{-2}\frac{\partial p'}{\partial z} - g\theta' = 0. \tag{2.20}$$

Finally, the linearised mass conservation and thermodynamic equations are

$$\frac{\partial u'}{\partial x} + \frac{\partial v'}{\partial y} + \frac{\partial w'}{\partial z} = 0 \tag{2.21}$$

$$\frac{\partial \theta'}{\partial t} + w'\frac{\partial \overline{\theta}}{\partial z} = 0 \tag{2.22}$$

respectively.

We see that the Froude number has not yet been introduced into the equations. To do this we take $\frac{\partial}{\partial t}$ of Eq. (2.20), giving

$$\frac{\partial^2 w'}{\partial t^2} + A^{-2}\frac{\partial^2 p'}{\partial z \partial t} - g\frac{\partial \theta'}{\partial t} = 0.$$

Substituting in for $\frac{\partial \theta'}{\partial t}$ from Eq. (2.22) gives

$$\frac{\partial^2 w'}{\partial t^2} + A^{-2}\frac{\partial^2 p'}{\partial z \partial t} + w'g\frac{\partial \overline{\theta}}{\partial z} = 0.$$

We now define

$$Fr^{-2} = g\frac{\partial \overline{\theta}}{\partial z}A^2$$

and note that

$$N^2 = g^*\frac{\partial \overline{\theta}}{\partial z^*} = T^{-2}Fr^{-2}A^{-2}$$

so

$$Fr^{-2} = N^2T^2A^2 = \frac{N^2H^2}{U^2} \qquad \Rightarrow \qquad Fr = \frac{U}{NH}.$$

So Fr has been introduced into the equations after linearisation. Solutions of the nonlinear equations will thus depend only on Ro, A and g. If the linearisation is accurate, the solution will depend on Ro, A and Fr.

2.2 Solution of the linearised equations

We now assume solutions of the form

$$\begin{aligned} u &= \hat{u}\, e^{i(\omega t+kx+ly+mz)} \\ v &= \hat{v}\, e^{i(\omega t+kx+ly+mz)} \\ w &= \hat{w}\, e^{i(\omega t+kx+ly+mz)} \\ p &= \hat{p}\, e^{i(\omega t+kx+ly+mz)} \\ \theta &= \hat{\theta}\, e^{i(\omega t+kx+ly+mz)} \end{aligned}$$

and upon substitution these give

$$\begin{aligned} i\omega\hat{u} + ik\hat{p} - f\hat{v} &= 0 \\ i\omega\hat{v} + il\hat{p} + f\hat{u} &= 0 \\ i\omega\hat{w} + im\hat{p} - \frac{g\hat{\theta}}{\theta_0} &= 0 \\ ik\hat{u} + il\hat{v} + im\hat{w} &= 0 \\ i\omega\hat{\theta} + \frac{\partial\overline{\theta}}{\partial z}\hat{w} &= 0. \end{aligned}$$

Non-trivial solutions to this system of equations are given by

$$\det\begin{vmatrix} i\omega & -f & 0 & ik & 0 \\ f & i\omega & 0 & il & 0 \\ 0 & 0 & i\omega & im & -\frac{g}{\theta_0} \\ ik & il & im & 0 & 0 \\ 0 & 0 & \frac{\partial\overline{\theta}}{\partial z} & 0 & i\omega \end{vmatrix} = 0.$$

We assume that $N^2 \equiv \frac{g}{\theta_0}\frac{d\overline{\theta}}{dz}$ is independent of z and we obtain

$$-i\omega^3(k^2+l^2+m^2) + i\omega f^2 m^2 + i\omega(k^2+l^2)N^2 = 0$$

$$\Rightarrow \qquad \omega = 0 \qquad \text{or} \qquad \omega = \pm\sqrt{\frac{f^2m^2+(k^2+l^2)N^2}{k^2+l^2+m^2}}. \tag{2.23}$$

We now define a characteristic time scale $T = \omega^{-1}$, horizontal length scale $L = (k^2+l^2)^{-\frac{1}{2}}$ and height scale $H = m^{-1}$. Three cases of (2.23) can be investigated as follows:

Case 1: $m^2 \gg k^2+l^2$ *and* $f^2m^2 \gg (k^2+l^2)N^2 \qquad (L/H \gg 1)$

In this case the solution reduces to

$$\omega = \pm\sqrt{\frac{f^2m^2}{m^2}} \quad \Rightarrow \quad \omega = \pm f \quad \Rightarrow \quad T = \pm f^{-1}$$

leading to shallow disturbances such as inertial waves.

Case 2: $m^2 \ll k^2+l^2$ *and* $f^2m^2 \ll (k^2+l^2)N^2 \qquad (L/H \ll 1)$

In this case the solution reduces to

$$\omega = \pm\sqrt{\frac{(k^2+l^2)N^2}{k^2+l^2}} \quad \Rightarrow \quad \omega = \pm N \quad \Rightarrow \quad T = \pm N^{-1}$$

leading to deep disturbances such as buoyancy oscillations.

Case 3: $m^2 \gg k^2 + l^2$ *but* $f^2 m^2 \ll (k^2 + l^2)N^2 \qquad (L/H \gg 1)$

In this case the solution reduces to

$$\omega = \pm\sqrt{\frac{(k^2 + l^2)N^2}{m^2}} \quad \Rightarrow \quad \frac{\omega}{\sqrt{k^2 + l^2}} = \frac{N}{m}$$

leading to internal gravity waves.

We expect these solutions to be typical of the wave solutions of the fully compressible equations.

2.3 Description of the semi-geostrophic solution

Shutts (1998) describes a semi-geostrophic model of upstream blocking. The semi-geostrophic solution shows a blocked region and barrier jet upstream of the mountain. High potential temperature air is forced to descend on the lee side of the mountain. He states that isentropes that were initially level with the mountain top may be pulled right down to the lowest level. He assumes that fluid instantaneously jumps from mountain crest height to a new downstream position conserving absolute momentum, and such a process involves the creation of unbalanced motion which must be dissipated. He further states that this energy dissipation occurs with a hydraulic jump near the leading edge of the downstream fluid. The rate of energy dissipation is equal to the pressure drag on the mountain. This can be calculated from the hydrostatic pressure difference resulting from the difference between the potential temperature of the summit level air which is blocked by the mountain and that of the air at the mountain top which is pulled down on the downstream side. This drag is thus independent of the wind speed.

Chapter 3

Steady State Experiments

3.1 Overview of the model

The experiments in this project are conducted using a vertical slice version of the Met Office Unified model. The model makes use of a semi-implicit integration scheme and semi-Lagrangian advection (Cullen *et al.* 1997). There is no CFL criterion and so in the scheme u_j does not depend upon its immediate neighbours and thus there is no restriction on Δt. The idea of semi-Lagrangian schemes is to achieve stability even for large Δt by choosing the most appropriate interval for interpolation, so satisfying the CFL criterion. However, stability is still limited by a trajectory crossing condition. Some disadvantages of semi-Lagrangian schemes are that more computer time is required per time step, they are not particularly accurate with fast forcing such as semi-implicit gravity waves and they are overly diffusive on coarse grids.

Other features of the model are the inclusion of non-hydrostatic effects and the use of a semi-implicit algorithm for solving the fully compressible equations. Finite differences are used and the 'Charney-Phillips' vertical arrangement of variables (Fig. 3.1) is used to improve the geostrophic adjustment properties (Cullen *et al.* 1997).

The time integration scheme used in the model is based on the second order implicit Trapezoidal scheme

$$u^{n+1} = u^n + \frac{\Delta t}{2}[F(u^{n+1}) + F(u^n)]$$

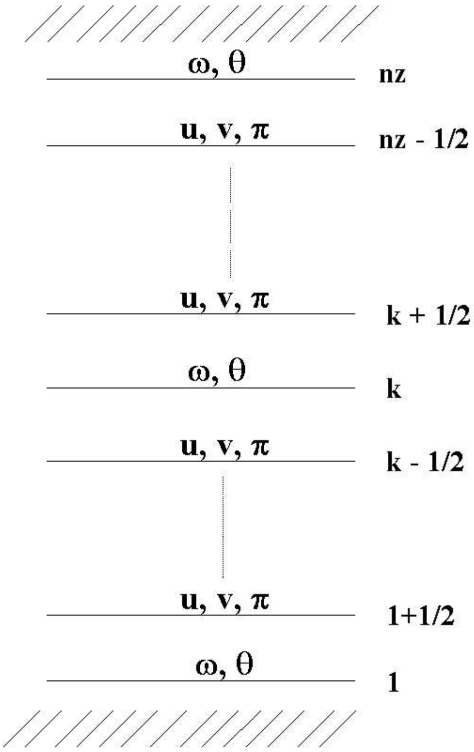

Figure 3.1: *Position of the variables of the Charney-Phillips grid where* π = *Exner pressure (taken from Cullen et al. (1997)).*

which is then generalised by

$$u^{n+1} = u^n + \frac{\Delta t}{2}[\alpha F(u^{n+1}) + (1-\alpha)F(u^n)]$$

where α is a weighting parameter between 0 and 1. Three choices of α can occur as follows:

$\alpha < \frac{1}{2}$	unstable
$\alpha = \frac{1}{2}$	scheme 2^{nd} order accurate
$\alpha > \frac{1}{2}$	damping occurs.

In this model the orography is grown in the first part of the run to ensure a smooth start.

3.2 Choice of CFL and α

An important consideration in all numerical modelling is how computationally expensive the model is, i.e. how much computer time is needed to achieve the required result. In the model used here the value of the CFL number determines the timestep. A larger CFL number will give a larger timestep. We obviously want to use as little computer time as possible and so we want to find the least number of timesteps and the longest timestep necessary for steady state, i.e. the solution in which the fields no longer vary with time. We require this steady state in order to see the response to the presence of the ridge.

The value of the weighting parameter α will also affect how quickly the solution reaches steady state. As stated in the previous section damping of the solution occurs for $\alpha > \frac{1}{2}$. So in this section we set the Coriolis parameter f to zero and investigate different values of CFL and α to see which combination gives the fastest convergence to steady state.

Values of CFL investigated here are 0.2 and 0.4. Higher values were tried but these caused the model to fail in the region of strong downslope winds. Values of α investigated are 0.8 and 1.0. To keep each experiment consistent we keep the product of CFL and the number of timesteps for the orography to grow to its final height, equal to 20. Thus for CFL $= 0.2$ the orography takes 100 timesteps to grow, and for CFL $= 0.4$ it takes 50 timesteps to grow.

Figure 3.2 shows graphs of how the u and w fields for each combination of CFL and α tend to steady state. We can see that for CFL $= 0.4$ the differences in the fields between time steps are less than for CFL $= 0.2$ from 150 time steps and from here these differences remain small and reasonably constant. Thus the solution tends to steady state in a lesser number of timesteps than for CFL $= 0.2$. Also, for CFL $= 0.4$ and for $\alpha = 1.0$ steady state is reached at the same time as for $\alpha = 0.8$ but the difference in each field between timesteps is slightly less.

For subsequent experiments in this project we therefore choose standard values of CFL $= 0.4$ and $\alpha = 1.0$.

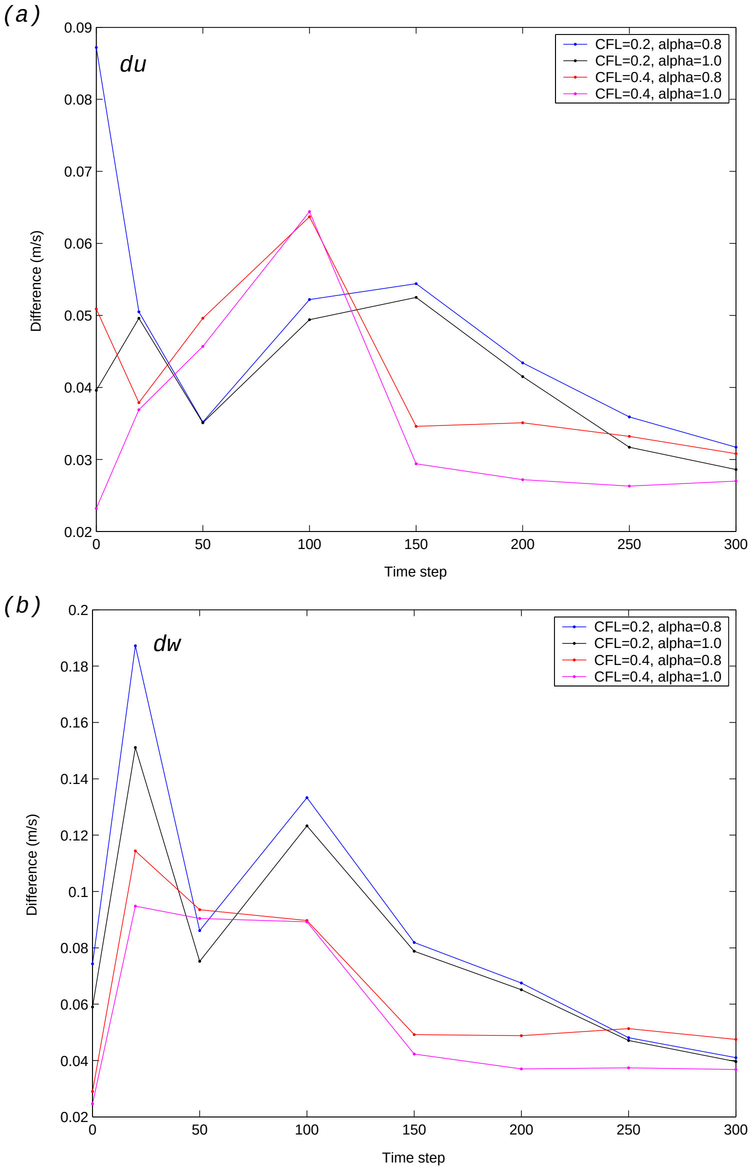

Figure 3.2: *Timesteps for solution to reach steady state for (a) u field and (b) w field. The values of CFL and* α *for each experiment are given in the legend.*

3.3 Steady state for $f \to 0$

In these experiments we now switch rotation on and attempt to find the steady state solution of flow over an isolated cosine hill of half-width $L = 300km$ and height $H = 2400m$. In the vertical the model has 20 levels with a grid length of $0.5km$. The horizontal grid length is $50km$.

For the steady state solution ($\frac{Dv}{Dt} = \frac{\partial v}{\partial t} + u\frac{\partial v}{\partial x} + w\frac{\partial v}{\partial z} = 0$) our y-component equation of motion (2.2) becomes

$$fU = -\frac{1}{\rho}\frac{\partial p}{\partial y} \tag{3.1}$$

where U is the wind speed in the x direction. As we keep U at a constant value of $10ms^{-1}$ and vary f we must also vary the right-hand side of (3.1) by the same factor so as to always keep the equation in balance. For example, if we halve the value of f we must also halve the value of the right-hand side.

From the linear analysis in Section 2.2 we can say that *Case 1* is applicable here because our mountain half-width $L = 300km$ and mountain height $H = 2400m$ ($L/H \gg 1$). This gave a characteristic timescale $T = f^{-1}$. The time to reach geostrophic balance will be of order this timescale and so the time for the solution to reach steady state should be a few times f^{-1}. This will increase with decreasing values of f and decrease with increasing values of f. However, the downstream flow is turbulent and so the solution will never reach steady state.

Table 3.1 gives the values of f used in this experiment. A value of $f = f_0/6$ was also tried but this solution did not converge to a steady state. Increasing the domain length further may have solved this problem but then the experiment would become too computationally expensive.

Table 3.1: *Values of f used in experiment.*

f	Value	f^{-1} (hr)
$2f_0$	$2.5260 \times 10^{-4} s^{-1}$	1.1
f_0	$1.2630 \times 10^{-4} s^{-1}$	2.2
$f_0/2$	$0.6315 \times 10^{-4} s^{-1}$	4.4
$f_0/4$	$0.3158 \times 10^{-4} s^{-1}$	8.8
zero	0.0	-

For $f = 2f_0$ and f_0 the length of the domain is $4000km$ with the mountain centred at $2000km$. For $f = f_0/2$ the domain length is also $4000km$ but with the mountain centred at $2500km$ to ensure that the region of upstream influence (discussed later in Section 4.2) does not interfere with the left-hand boundary. For $f = f_0/4$ the domain length is $6000km$ with the mountain centred at $3000km$, again to allow for the region of upstream influence.

The steady state for a particular value of f is found by calculating the difference in a particular field between successive timesteps for only the left half of the domain where there are no turbulent features. For example, the difference in the u field is calculated using

$$\Delta u = \sqrt{\frac{\sum_{i=1}^{I} (u_i^t - u_i^{t+\Delta t})^2}{I}} \tag{3.2}$$

where I is the number of u values in the domain.

In the model the orography is ‘grown’ from nothing to its final height in 50 timesteps. Therefore steady state can certainly not be reached before this time. For $f = 2f_0, f_0, f_0/2$ the timestep is $2025s$ and so the mountain is fully grown in $28.1hr$. For $f = f_0/4$ the timestep is $2017s$ and the mountain is fully grown in $28.0hr$. Figure 3.3 shows graphs

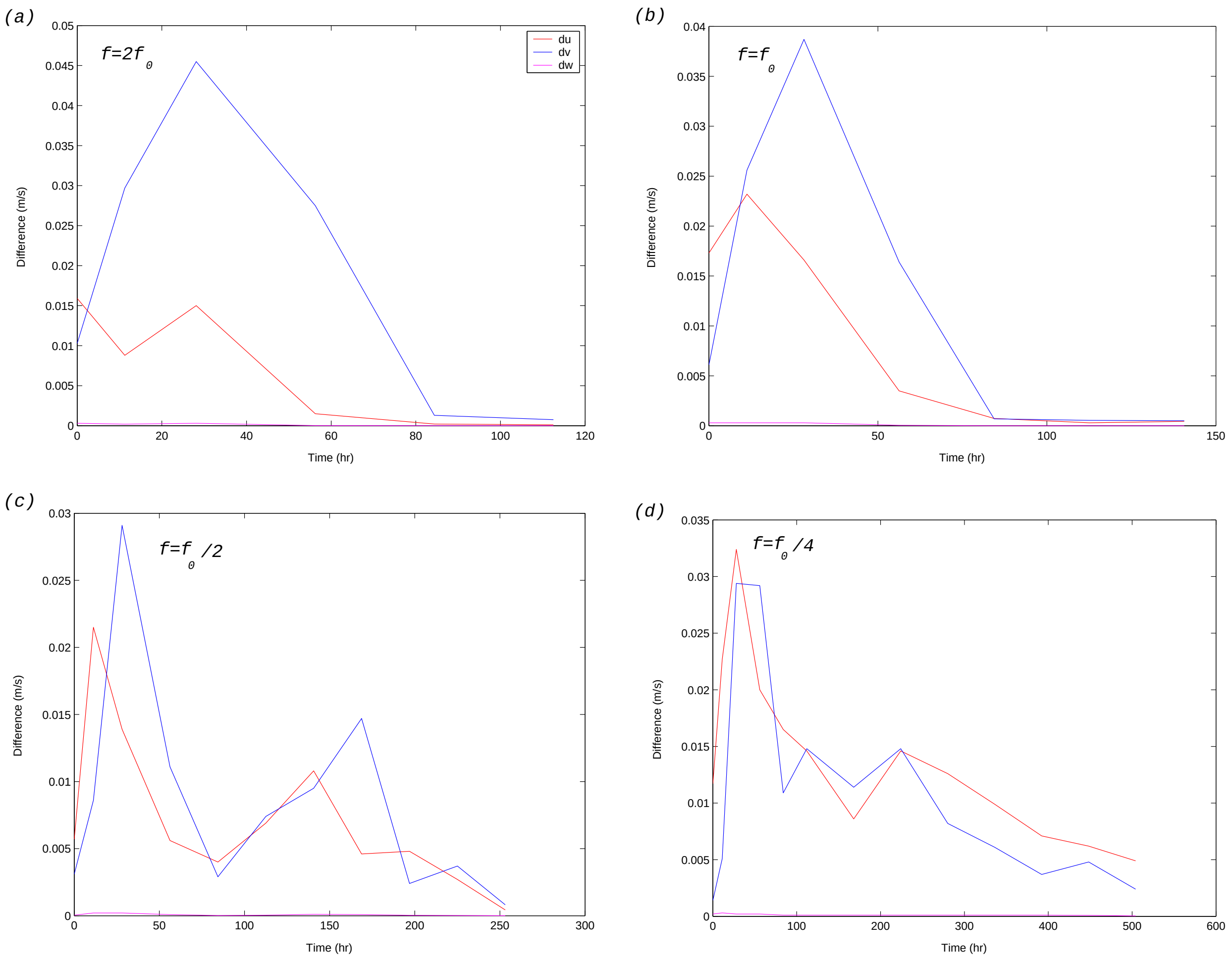

Figure 3.3: *Times for solution to reach steady state for (a)* $2f_0$*, (b)* f_0*, (c)* $f_0/2$ *and (d)* $f_0/4$*. The legend shown in (a) applies to all graphs.*

of how the u, v and w fields for each f tend to steady state. For $f = 2f_0, f_0, f_0/2$ the steady states are taken to be $112hr$ (200 timesteps), $112hr$ and $253hr$ (450 timesteps) respectively. For $f = f_0/4$ the steady state is taken to be $504hr$ (900 timesteps).

3.4 Steady state for $U \rightarrow 0$

For this experiment our equation of motion (3.1) still applies but this time we are keeping f at a constant value of $f_0 = 1.2630 \times 10^{-4}s^{-1}$ and varying U towards zero. The same principle applies here as in the previous section in that if we halve the value of U we must also halve the value of the right-hand side.

Table 3.2: *Values of U used in experiment.*

U	Value
$2U_0$	$20ms^{-1}$
U_0	$10ms^{-1}$
$U_0/2$	$5ms^{-1}$
$U_0/4$	$2.5ms^{-1}$

Again, the time for the solution to reach steady state should be a few times f^{-1} and only the left half of the domain is considered when using (3.2).

Table 3.2 gives the values of U used in this experiment. The timestep is also determined by the value of U and so it is still necessary to do the steady state experiments even though f is being held constant. The model would not run for values of U smaller than $2.5ms^{-1}$ which may be due to the timestep becoming too large for the given Courant number. For $U = 2U_0, U_0, U_0/2, U_0/4$ the timesteps are $1012s$, $2025s$, $4050s$ and $8101s$ respectively. Therefore the times for the mountain to fully grow are $14.1hr$, $28.1hr$, $56.3hr$ and $112.0hr$ respectively.

Figure 3.4 shows graphs of how the u, v and w fields for each U tend to steady state. For $U = 2U_0, U_0, U_0/2, U_0/4$ the steady states are taken to be $112hr$ (400 timesteps), $112hr$ (200 timesteps), $112hr$ (100 timesteps) and $338hr$ (150 timesteps) respectively. Note that for the first three the time to reach steady state is the same since we are not varying f, which is what this timescale depends on. However, this is not the case for $U = U_0/4$ because, as stated above, the mountain has only just finished growing at $112hr$ and so a longer time is needed to reach a satisfactory steady state.

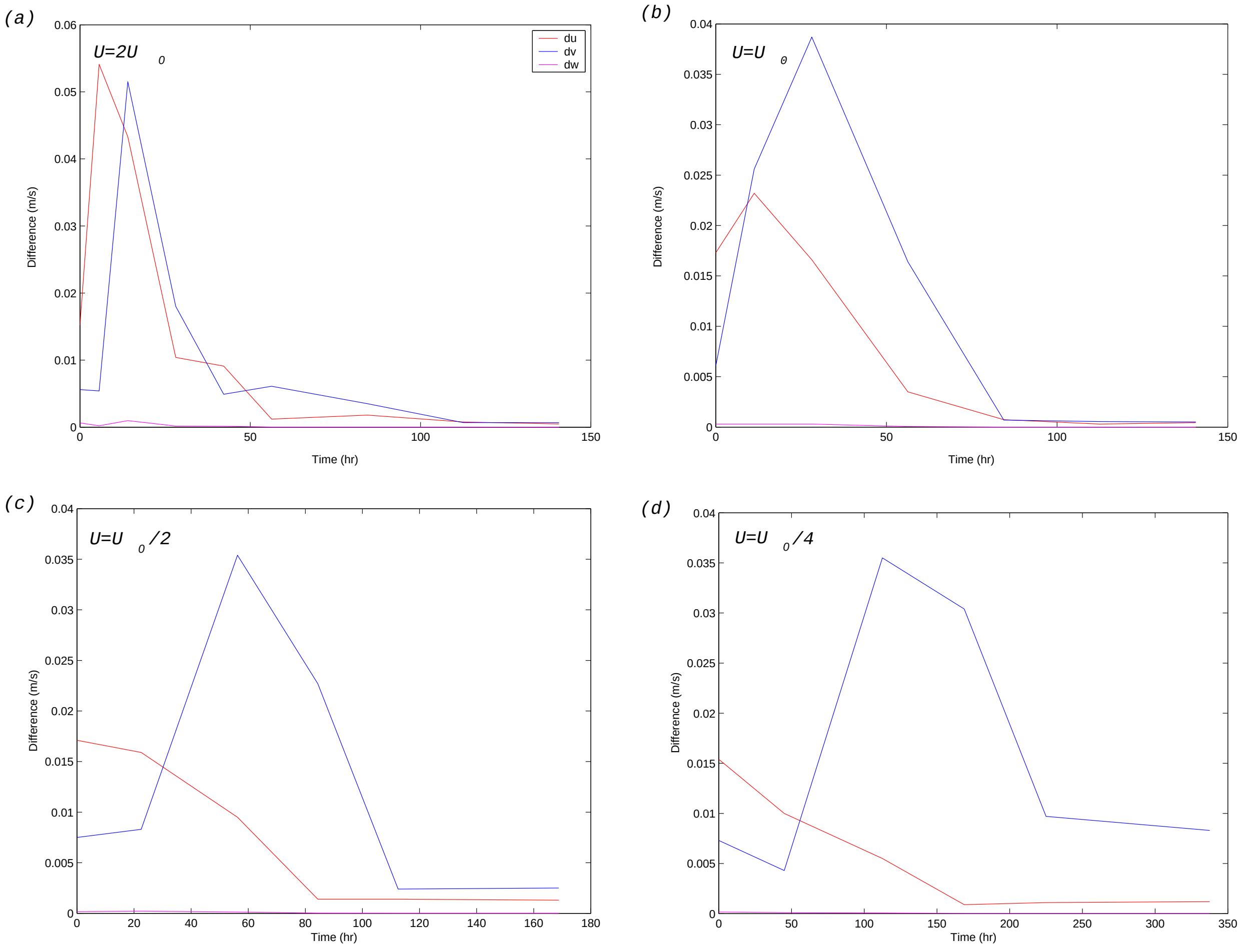

Figure 3.4: *Times for solution to reach steady state for (a) $2U_0$, (b) U_0, (c) $U_0/2$ and (d) $U_0/4$. The legend shown in (a) applies to all graphs.*

Chapter 4

Sensitivity of Solution for $f \to 0$

4.1 Singularity of the limit $f \to 0$

As the Coriolis parameter f decreases we might expect the steady state solution to converge towards the $f = 0$ state. Sprenger and Schär (2001) however, found that this is not the case. They conducted numerical experiments with values of $f = f_0$, $f_0/3$, $f_0/6$ and $f_0/12$. The flow fields for the $f_0/6$ and $f_0/12$ experiments displayed negligible difference and so their results demonstrated that the limit $f \to 0$ is singular, i.e the flow fields did not converge with decreasing f towards the $f = 0$ state. This can be explained by looking back at our steady state equation of motion (3.1). Even if there is a weak f there is still a weak pressure gradient leading to flow in the y direction, whereas for the $f = 0$ state there is no pressure gradient and so no flow in the y direction.

Sprenger and Schär (2001) also conducted an experiment with $f = -f_0/12$ which produced the same solution as for the $f = f_0/12$ case, except for a change in sign. They therefore hypothesised that in the absence of rotation the flow problem has multiple solutions; one for $f = 0$ and two obtained in the limits $f \to 0^+$ and $f \to 0^-$.

We now look at how the results of the numerical experiments in this project compare with the above theory. Figure 4.1 shows the steady state v fields for the f values discussed in Section 3.3. A plot for the $f = 0$ case is not shown since v is zero everywhere.

We see that a pronounced v wind continues to exist in the form of a barrier jet (dis-

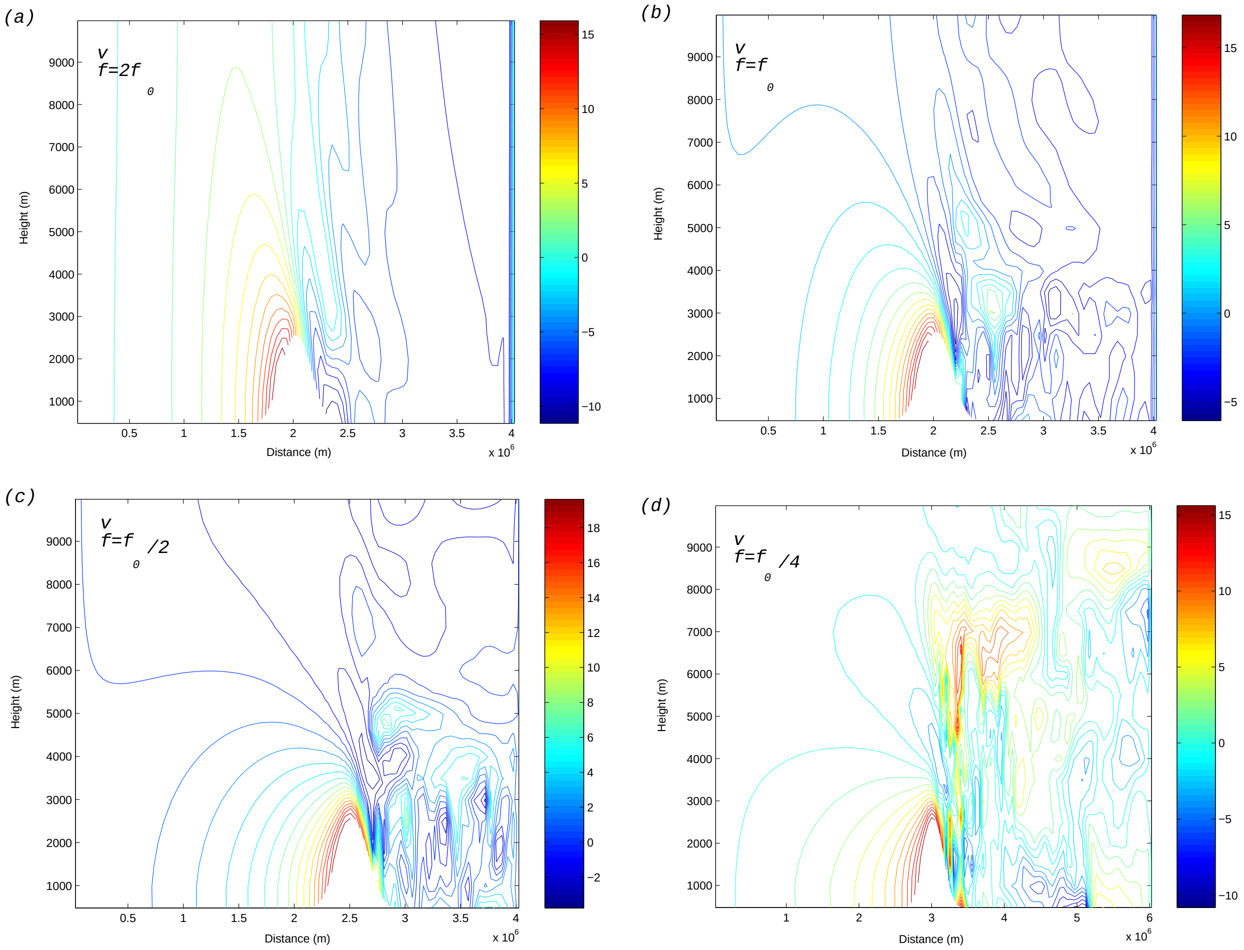

Figure 4.1: *Steady state* v *fields for (a)* $2f_0$*, (b)* f_0*, (c)* $f_0/2$ *and (d)* $f_0/4$*. Contour values are in accordance with the colour bar in* ms^{-1}.

cussed in Section 4.2) even for $f = f_0/4$. It is clearly not converging to the $f = 0$ state, i.e. zero v wind everywhere. An experiment with $f = -f_0/4$ was also carried out and this produced the same v field as for the $f = f_0/4$ case except for a change of sign. We therefore also hypothesise that the limit $f \to 0$ is singular and has multiple solutions.

4.2 Variation of upstream influence with f

Upstream blocking has been recognised as a feature of mountain flows for many years. If the Froude number (1.1) of a stratified flow over a (two-dimensional) obstacle is sufficiently large, fluid near the ground would be blocked on the upstream and not flow over the obstacle. In particular, for two-dimensional topography when U and N are constant with height, the criterion for blocking is $NH/U \gtrsim 2$ (Baines 1987). In the presence of rotation the air trajectories within the blocked region may be substantially deflected laterally from those at higher levels (Shutts 1998) and thus take the form of a barrier jet on the upstream side of the obstacle. This region of blocking, or upstream influence, is of the order of the Rossby radius of deformation L_R (4.1).

$$L_R = \frac{NH}{f} \tag{4.1}$$

The distance L_R is taken from the centre of the mountain as shown in Fig. 4.2.

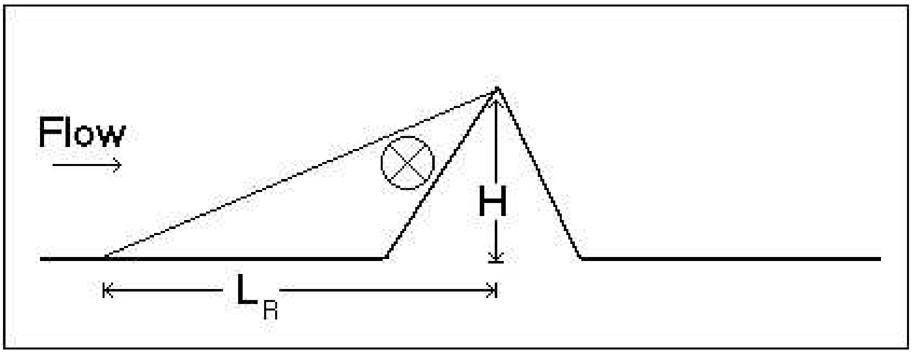

Figure 4.2: *Schematic showing the upstream blocking of a mountain, height H, and barrier jet (indicated by the $\otimes$). The extent of the blocking is the distance L_R.*

In the nonrotating case a mountain with sufficiently large Froude number generates an upstream blocked layer of infinite extent. However, in the rotating case the blocked region can extend far upstream when the Coriolis forces are small (Pierrehumbert and Wyman

1985). We can see from (4.1) that as f decreases L_R increases and so as $f \to 0$, $L_R \to \infty$. Similar results were found by Cullen *et al.* (1987). They conducted experiments with a stratified flow over a mountain barrier and in the absence of rotation they found no limit on the upstream influence as dense air was blocked by the mountain. With rotation present the upstream influence was restricted to a finite distance.

We can also measure the distance of upstream influence using

$$\delta x = \frac{v_{max}}{f} \tag{4.2}$$

where δx is the distance that an air parcel is 'pushed back from where it wants to be' by the orography, and v_{max} is the maximum wind speed in the barrier jet. We again see that as f decreases, this distance increases.

We now compare our results with the above theory. To begin with we can see a well defined barrier jet for each f value in Fig. 4.1 in the form of high v values on the upstream side of the mountain. This immediately agrees with the theory.

The distance of upstream influence for each f is found by calculating the horizontal upstream distance from the centre of the mountain that the value of v decreases to 10% of it's maximum value in the jet. We shall call this model-produced distance L_m.

The variation of L_m with f is shown in Fig. 4.3 along with the theoretical deformation radius L_R as given by (4.1). Also shown is the variation of δx as calculated using (4.2) with the model-produced values of v_{max}.

We can see that the distance δx is in close agreement with the theoretical L_R and that it decreases as f increases, as it should do. However, the distance L_m follows the same trend but has much larger values. The difference between L_m and L_R is of the order $1000km$.

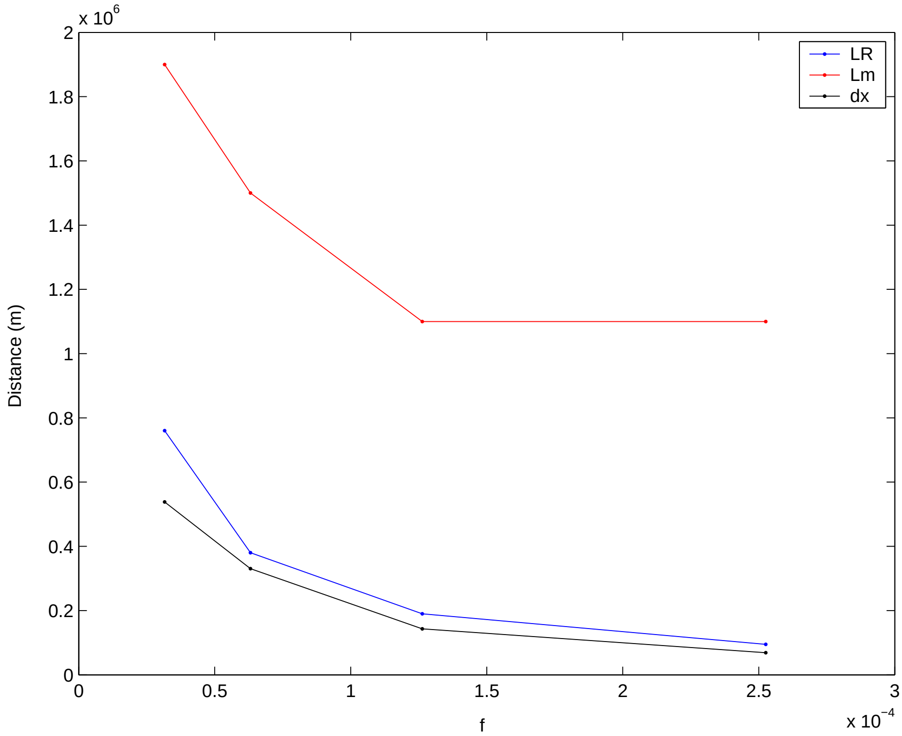

Figure 4.3: *Variation of Rossby radius of deformation* L_R*, model upstream influence* L_m *and model upstream distance* δx *with Coriolis parameter* f*.*

4.3 Variation of vertical kinetic energy with f

In experiments conducted by Sprenger and Schär (2001) it was found that the potential-temperature contours tilted upstream with height, indicating an upward transport of energy and a downward transport of momentum.

The vertical kinetic energy is given by

$$\text{vertical KE} = \int_V \frac{1}{2}\rho w^2\, dx\, dy\, dz \tag{4.3}$$

where V is the volume of the region of interest. We use this as a measure of gravity wave activity since the vertical KE is proportional to w^2 and we can conclude that as the amplitude of the displacements of potential temperature contours increase, so does the component of vertical velocity w.

The potential temperature and w fields for each f used in our numerical experiments are shown in Figs. 4.4 and 4.5 respectively.

We can see clearly defined vertically propagating gravity waves for each value of f (Fig. 4.4) and as f decreases the amplitude of the displacement of the isentropes appears to increase. The flow becomes more turbulent and is very turbulent for $f = f_0/4$ (Fig. 4.4(d)), however the flow for $f = 0$ (Fig. 4.4(e)) is not as turbulent as this. The w fields (Fig. 4.5) also clearly show the vertically propagating gravity waves and the maximum value of w appears to increase as f decreases. Therefore, we expect that as f decreases, the vertical kinetic energy increases.

A diagnostic calculation of the vertical kinetic energy is performed using (4.3). Above the mountain top the vertical KE of the balanced flow is negligible and so we use this as a measure of the gravity wave activity. Below the mountain top even the balanced flow implies large vertical KE. The region above the mountain over which we calculate the KE is the same size for each solution and is defined by

$$\begin{cases} 1 \times 10^6 m < x < 4 \times 10^6 m,\ 4000m < z < 10000m & f = 0, 2f_0, f_0, f_0/2 \\ 2 \times 10^6 m < x < 5 \times 10^6 m,\ 4000m < z < 10000m & f = f_0/4 \end{cases}$$

At each grid point in the region ρw^2 is evaluated and all values added together to calculate the total vertical KE. The variation of this energy with f is shown in Fig. 4.6.

As expected we see that the vertical KE increases as f decreases, however the value for $f = 0$ is less than that for $f_0/4$. This may be further evidence of the singularity of the limit $f \to 0$ (previously discussed in Section 4.1 in that the solution does not converge with decreasing f to the $f = 0$ state.

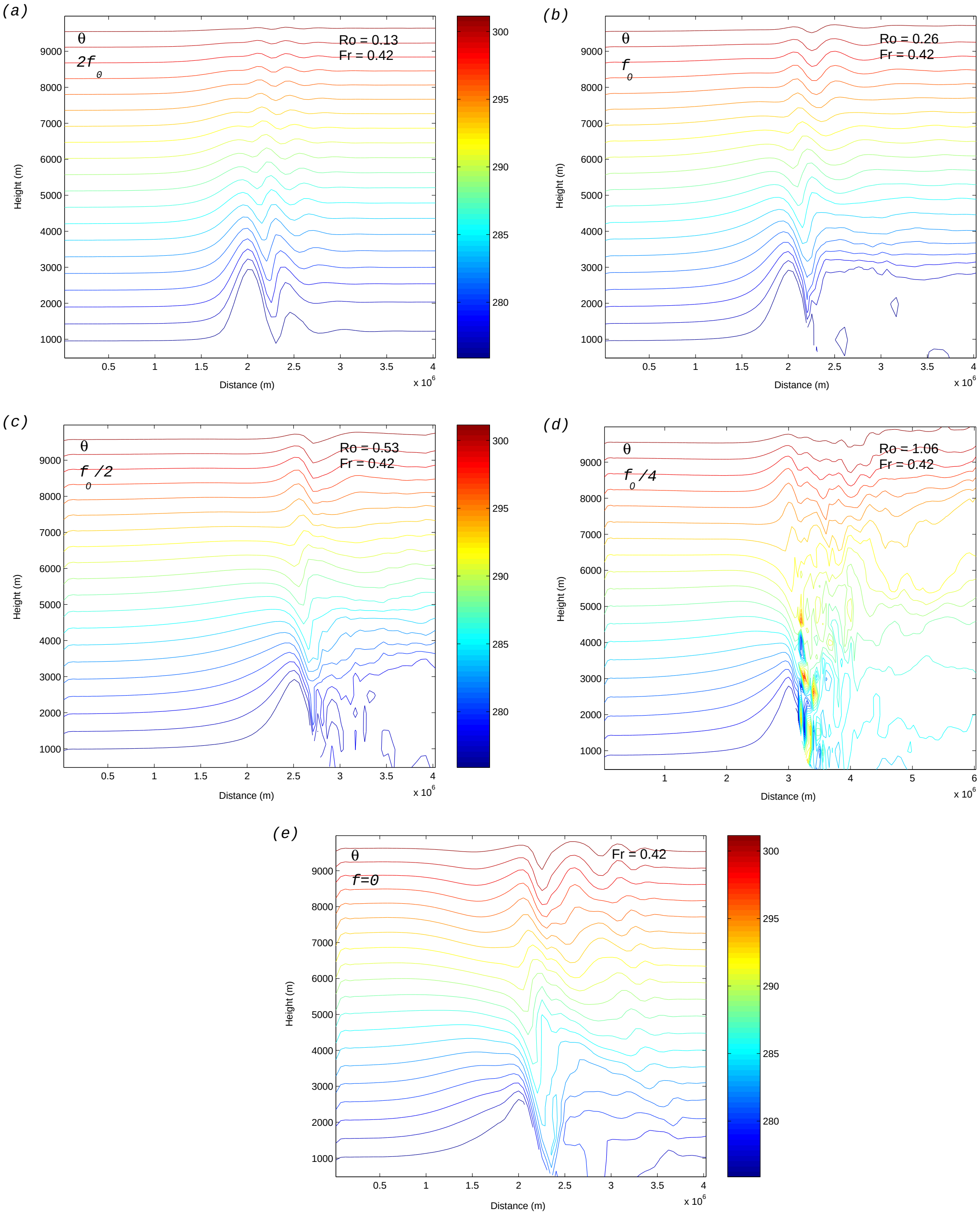

Figure 4.4: *Steady state θ fields for (a) $2f_0$, (b) f_0, (c) $f_0/2$, (d) $f_0/4$ and (e) $f = 0$. Contour values are in accordance with the colour bar in K.*

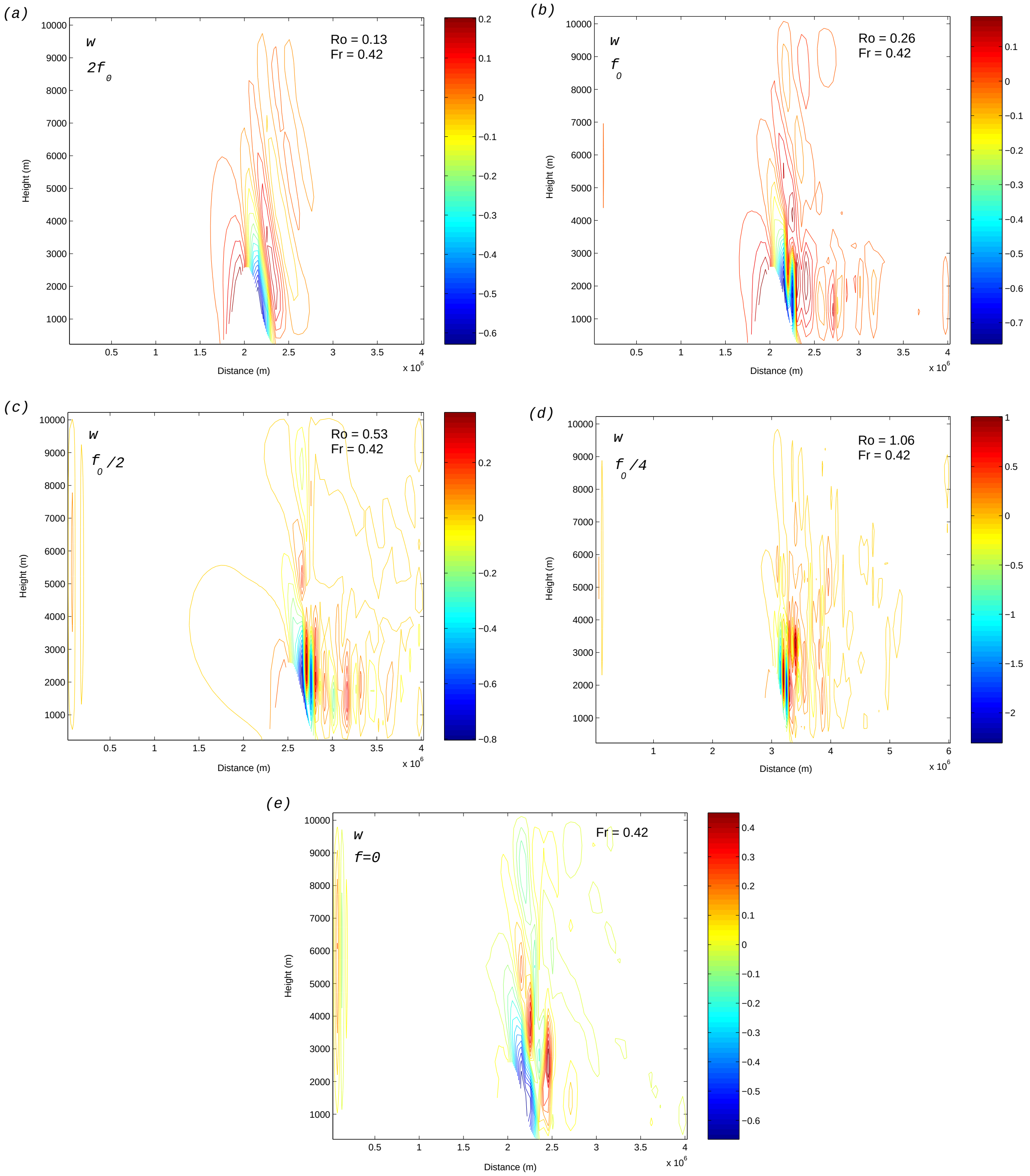

Figure 4.5: *Steady state w fields for (a) $2f_0$, (b) f_0, (c) $f_0/2$, (d) $f_0/4$ and (e) $f = 0$. Contour values are in accordance with the colour bar in ms^{-1}.*

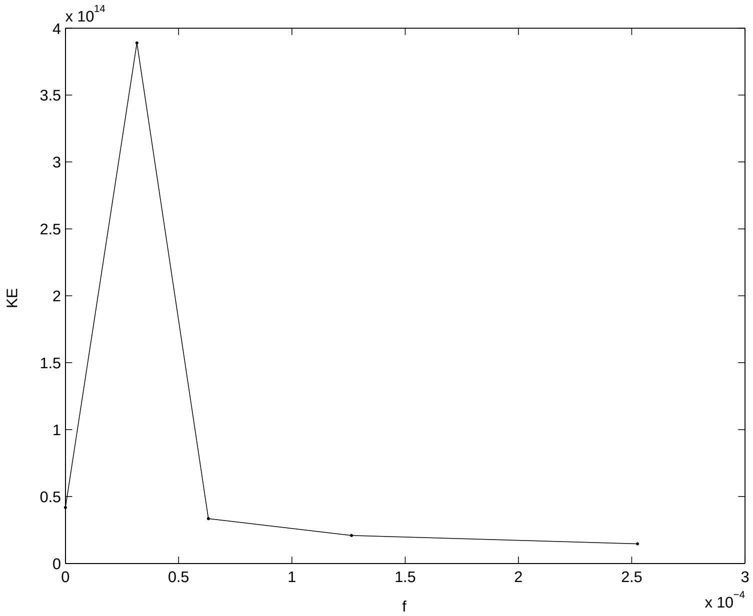

Figure 4.6: *Variation of vertical kinetic energy with Coriolis parameter f.*

4.4 Variation of pressure drag with f

Wind speed tends to be low on the windward slope of a mountain or ridge and faster on the leeward slope. From Bernoulli's equation, this requires a pressure difference across the mountain—high pressure upwind and lower pressure downwind (Smith 1979a) . The pressure difference results in a net drag on the mountain which can be computed as the horizontal pressure force on the mountain

$$D = \int_{-\infty}^{\infty} p(x, z = 0)\frac{dr}{dx}\, dx \tag{4.4}$$

where r is a height coordinate.

For the balanced solution there is drag due to upstream blocking (Shutts 1998), then for larger Ro there is additional wave drag.

The effect of rotation is to reduce the drag. As the parameter $Ro^{-1} = Lf/U$ increases, the flow gradually loses its wavelike character in the vertical plane (Smith 1979b). Ólafsson and Bougeault (1997) consider the fluid being decelerated as it approaches the mountain. The deceleration weakens the Coriolis force, and there is a net force acting to turn the flow left. Kinetic energy is transferred from flow in the x direction to flow in the y direction. The movement along the x axis sources the kinetic energy that counteracts the buoyancy force and forms the mountain wave. Therefore one may expect less pronounced waves in the presence of rotation.

In our experiments the drag on the mountain is calculated on the bottom row of the domain using an approximation to (4.4), i.e.

$$D = \sum_{i=0}^{\frac{J}{2}} p_i \left(\frac{r_{i+1} + r_i}{2} - \frac{r_{i-1} + r_i}{2} \right) - \sum_{i=\frac{J}{2}}^{J} p_i \left(\frac{r_{i+1} + r_i}{2} - \frac{r_{i-1} + r_i}{2} \right) \tag{4.5}$$

where $i = 0$ is the left hand edge of the mountain base, $i = J$ is the right hand edge of the mountain base and $\frac{J}{2}$ is the centre point of the mountain.

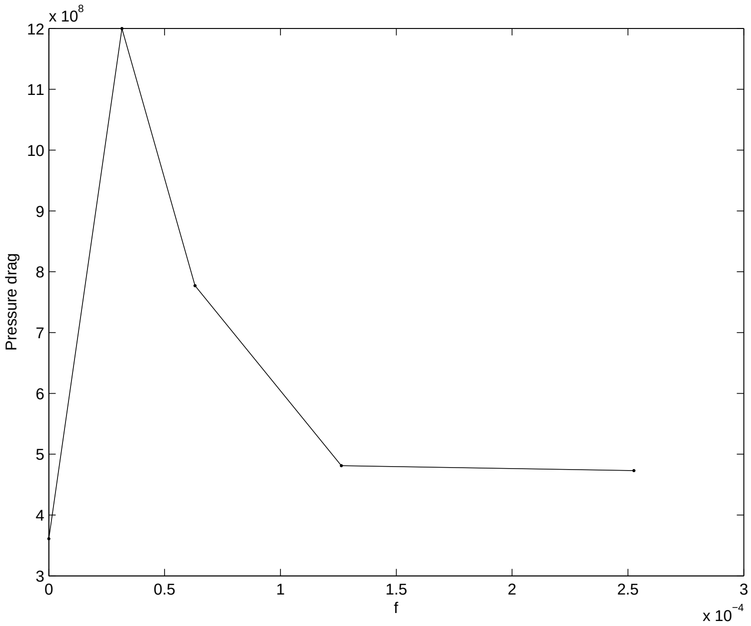

Figure 4.7: *Variation of the pressure drag across the mountain with Coriolis parameter f.*

From Fig. 4.7 we see that the pressure drag increases as f decreases as predicted, apart from when $f = 0$ when it is much less. This again may also be evidence of the singularity of the limit $f \to 0$.

Chapter 5

Sensitivity of Solution to upstream flow speed U

For the experiments in this chapter standard values of $f = f_0$ and $N = 0.01s^{-1}$ are used and U is varied according to the values given in Table 3.2. Thus as U decreases, Ro and Fr decrease at the same rate.

5.1 Variation of vertical kinetic energy with U

Smith (1979a) considers the limit of very slow wind speeds and strong stratification so that Fr is small. In this situation there will be little vertical motion and the fluid particles will deflect horizontally. He states that as Fr increases vertical deflections will occur. We could then argue that the vertical kinetic energy will also increase.

Sprenger and Schär (2001) conducted experiments in the rotating case where the upstream flow speed was varied from a standard value of $10ms^{-1}$ to values of $5ms^{-1}$ and $20ms^{-1}$. They noted that in general, a decrease of the upstream velocity inhibited wavelike features downstream. So we expect to find that as we decrease U, the amplitude of the displacement of the isentropes decreases. Thus the component of vertical velocity w should also decrease. In our experiments we again use (4.3) to calculate the vertical KE in a region above the mountain. We have said previously that this is a measure of gravity wave activity and so we should find that the vertical KE too decreases with decreasing values of U. We shall get the balanced solution as $Ro, Fr \to 0$ with Ro/Fr fixed.

The θ and w fields for each U used in our numerical experiments are shown in Figs. 5.1 and 5.2 respectively. Figure 5.1 clearly shows decreasing displacement amplitudes of the isentropes as U decreases. As the value of U becomes very small (Fig. 5.1(d)), Ro becomes very small and the solution gets closer to the steady state, wave-free semi-geostrophic solution.

From Fig. 5.2 we can see also the decreasing wave activity as U decreases. In fact the downward values of w on the immediate lee of the mountain decrease quite uniformly with decreasing U. Thus, quite logically, the föhn effects are almost negligible for small U values.

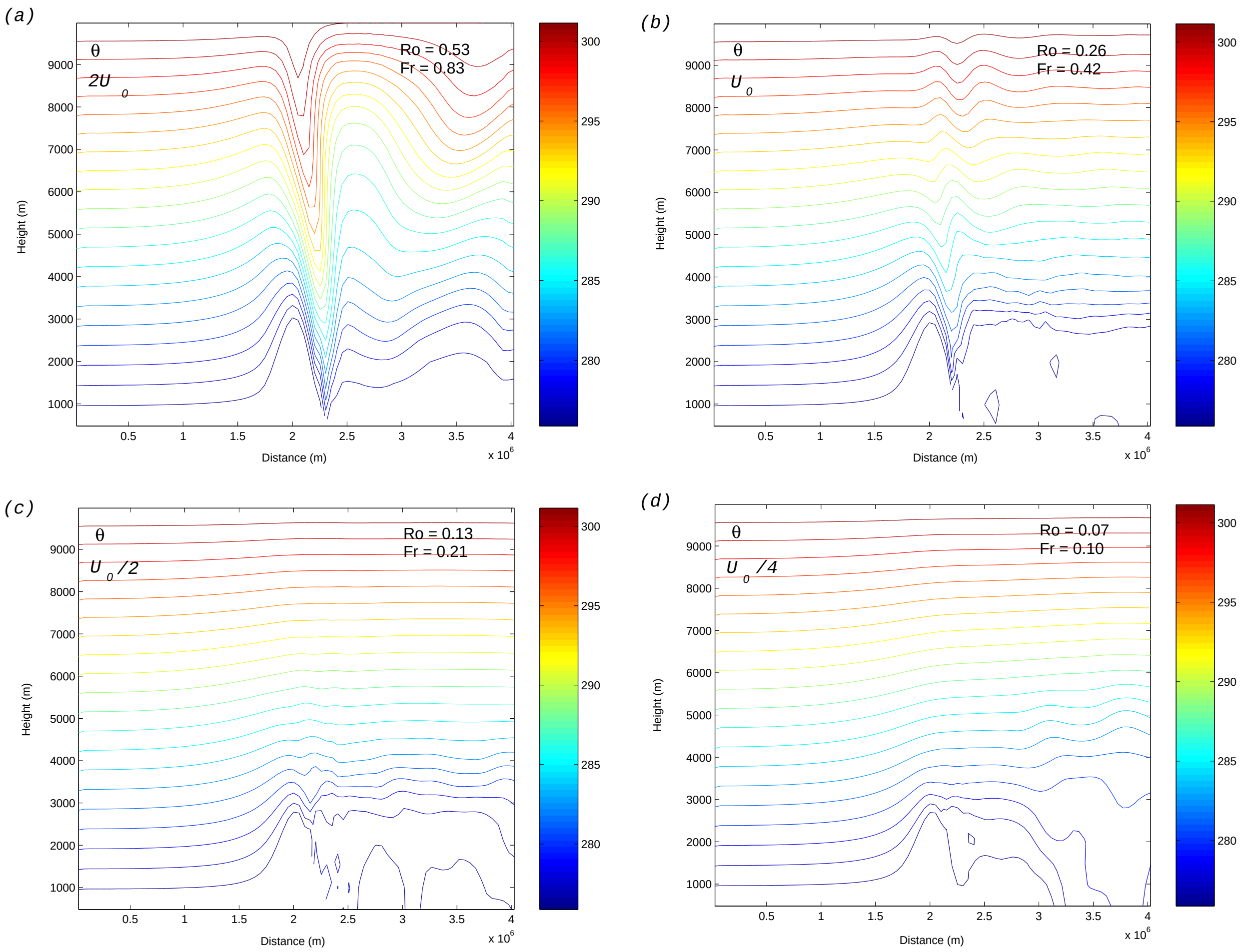

Figure 5.1: *Steady state θ fields for (a) $2U_0$, (b) U_0, (c) $U_0/2$ and (d) $U_0/4$. Contour values are in accordance with the colour bar in K.*

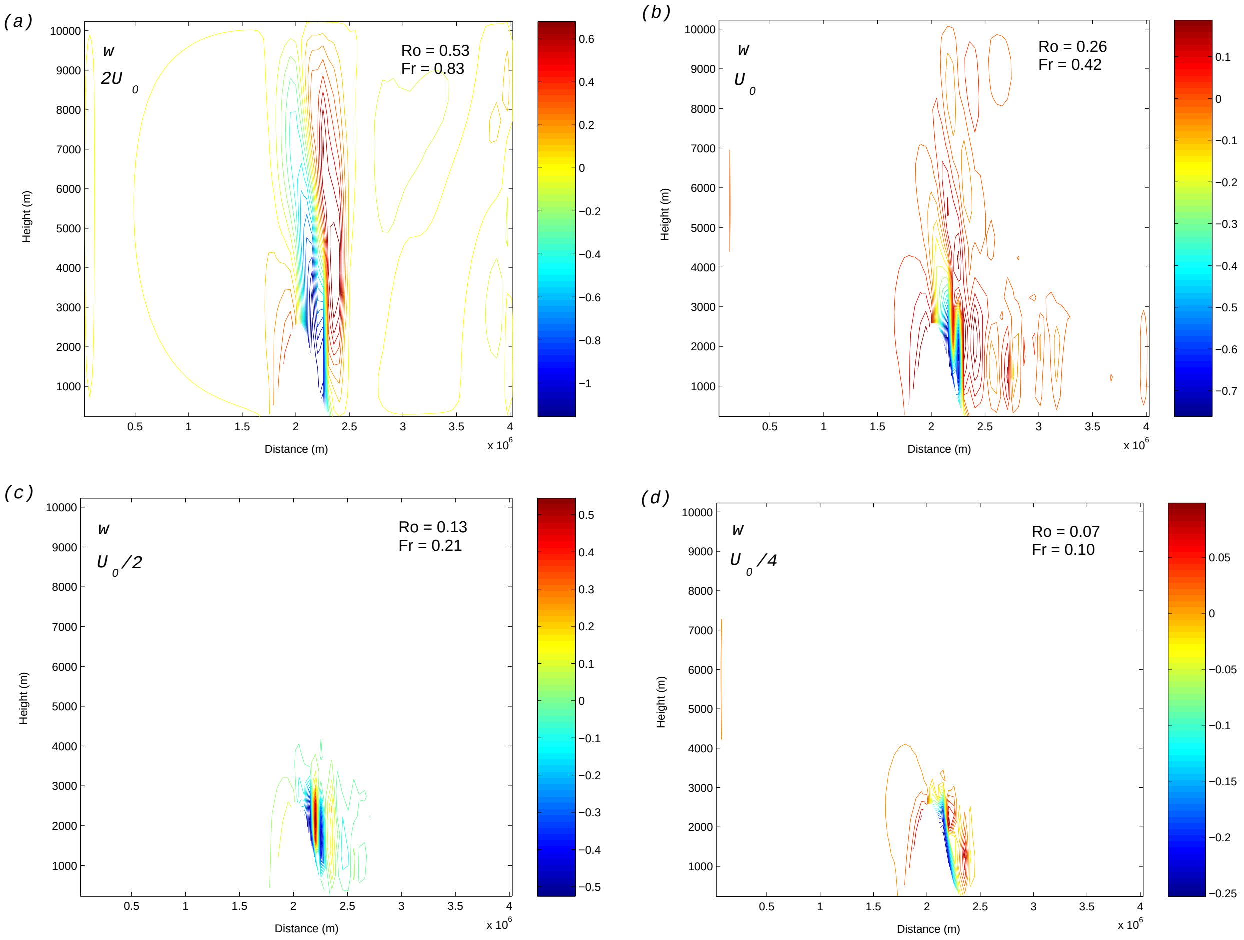

Figure 5.2: *Steady state* w *fields for (a)* $2U_0$*, (b)* U_0*, (c)* $U_0/2$ *and (d)* $U_0/4$*. Contour values are in accordance with the colour bar in* ms^{-1}.

The variation of vertical KE with U is shown in Fig. 5.3. As expected we see that this energy decreases as U decreases. It would be of interest to examine whether this variation conforms to a power law and so a plot of $\frac{1}{2}\,log\,KE$ versus $log\,U$ is also given (Fig. 5.4). The line of best fit through the points is given by the equation $\frac{1}{2}\,log\,KE = 2.468\,log\,U + 4.250$. We therefore have a relationship between $\sqrt{KE}$ and U given by the power law

$$\sqrt{KE} = U^{2.468} \times 10^{4.250}.$$

Due to the frontal scaling discussed previously in Chapter 1 this suggests second-order convergence to the semi-geostrophic solution.

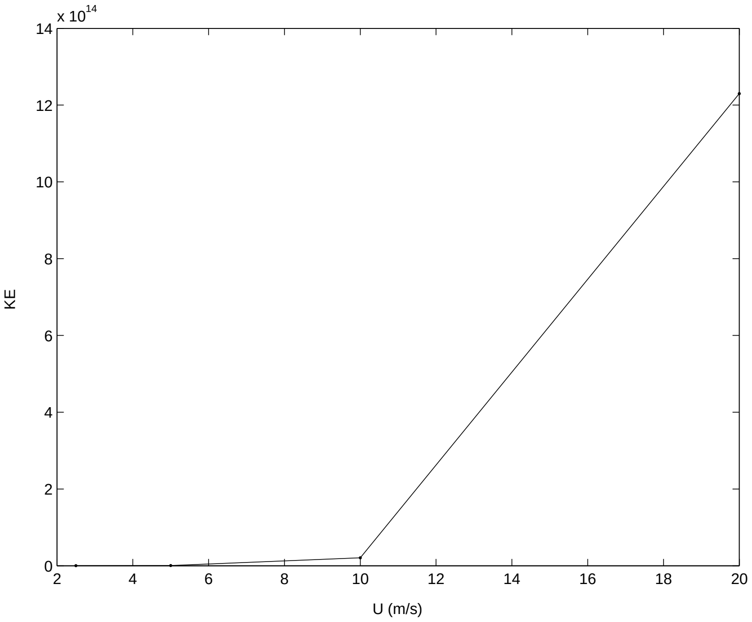

Figure 5.3: *Variation of vertical kinetic energy with upstream flow speed U.*

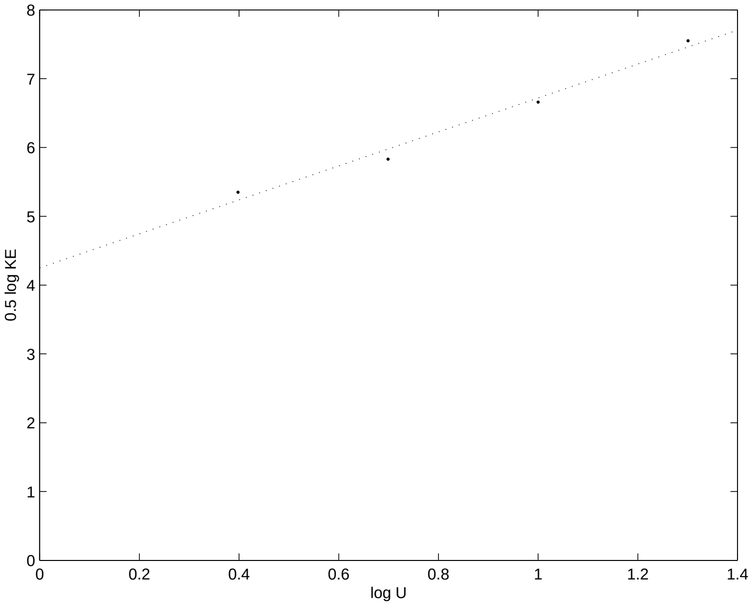

Figure 5.4: *Variation of $\frac{1}{2} \log KE$ with $\log U$. The equation of the line of best fit is* $\frac{1}{2} \log KE = 2.468 \log U + 4.250$.

5.2 Variation of pressure drag with U

In Section 4.4 we found that pressure drag increased as f decreased, i.e. as Ro increased. Since $Ro = U/fL$ and f remains constant in the experiments here, we could expect that as U increases, pressure drag also increases. Experiments conducted by Smith (1979b) showed that as the incident velocity decreased, so did the drag. This is indeed the case for our numerical experiments as shown in Fig. 5.5, yet it is only a weak dependence. Again Eq. (4.5) is used to compute the pressure force on the mountain. We see a reasonably linear relationship as U decreases from $20ms^{-1}$ to $5ms^{-1}$. However, the drag is slightly increased for $U = 2.5ms^{-1}$.

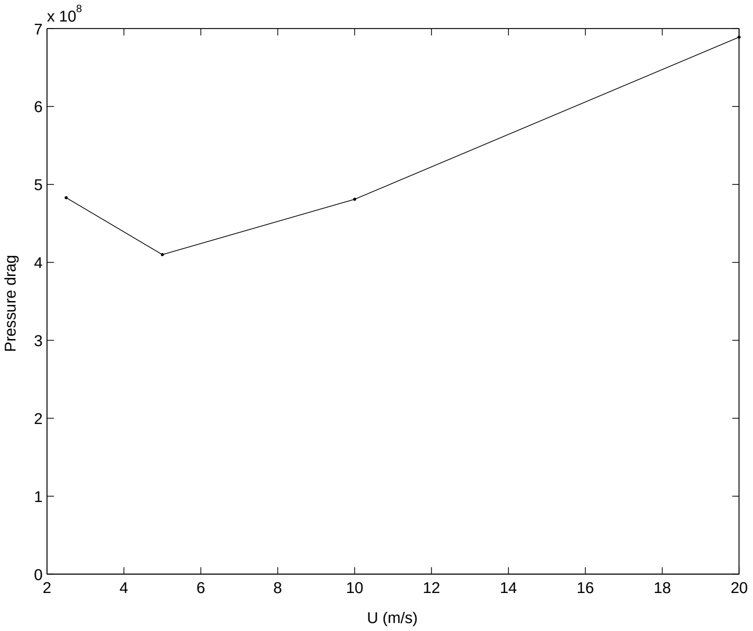

Figure 5.5: *Variation of the pressure drag across the mountain with upstream flow speed U.*

In the semi-geostrophic limit solution with very small U there is still drag because the mountain still blocks the oncoming flow, but as U (Ro) gets bigger the wave activity increases and there is drag due to the waves and also drag due to the semi-geostrophic solution. If $U = 0$ then there would be zero drag, but we did not have access to the code in which to compute the purely semi-geostrophic balance solution.

Chapter 6

Sensitivity of Solution to Rotation and Stratification

For the experiments in this chapter we vary the values of f and N but keep the value of the dimensionless parameter f/N constant. Using standard values of $f_0 = 1.263 \times 10^{-4} s^{-1}$ and $N_0 = 0.01 s^{-1}$ we get a value of $f/N = 0.01263$. Therefore, experiments are conducted using $2f_0$ and $2N_0$, f_0 and N_0, $f_0/2$ and $N_0/2$, and $f_0/4$ and $N_0/4$. Thus Ro and Fr increase at the same rate.

6.1 Effect on upstream influence distance and barrier jet

From the equation for the Rossby radius of deformation, L_R (4.1) we see that since we are keeping f/N constant, this theoretical value will remain at $190km$. In our experiments, the model distance of upstream influence, L_m, is calculated as described in Section 4.2 and the additional measure, δx (4.2) is also calculated. The variation of these are plotted against what we term the 'scaling factor' in Fig. 6.1 and the constant value of L_R is also shown for comparison. The scaling factor is just the factor of both f and N used in each experiment.

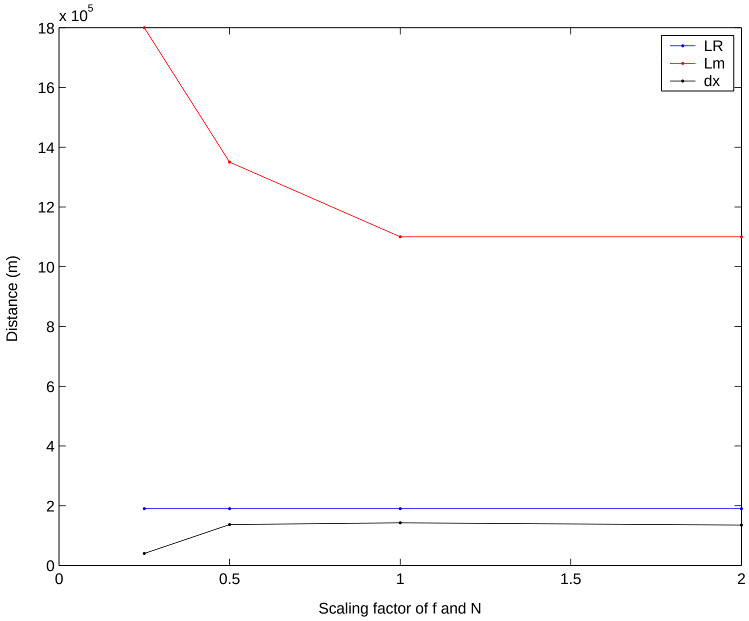

Figure 6.1: *Variation of distance of upstream influence with scaling factor (the factor by which both f and N are scaled in each experiment).*

We could argue that the $N = 2N_0, N_0, N_0/2$ values of L_m remain of a similar magnitude but the $N = N_0/4$ value is different. A possible explanation for this is that we may not have completely reached steady state for this value of f and thus the upstream influence has not settled at its steady state value. Also, for δx the $N = 2N_0, N_0, N_0/2$ values remain in close agreement with L_R but the $N = N_0/4$ value varies from the others by approximately 70%.

Figure 6.2 shows plots of the v component of wind for each experiment. We can immediately see that the strength of the barrier jet upstream of the mountain decreases as f and N are scaled down. Since we had to calculate v_{max} for the calculation of δx above we can now plot this as a function of the scaling factor (Fig. 6.3).

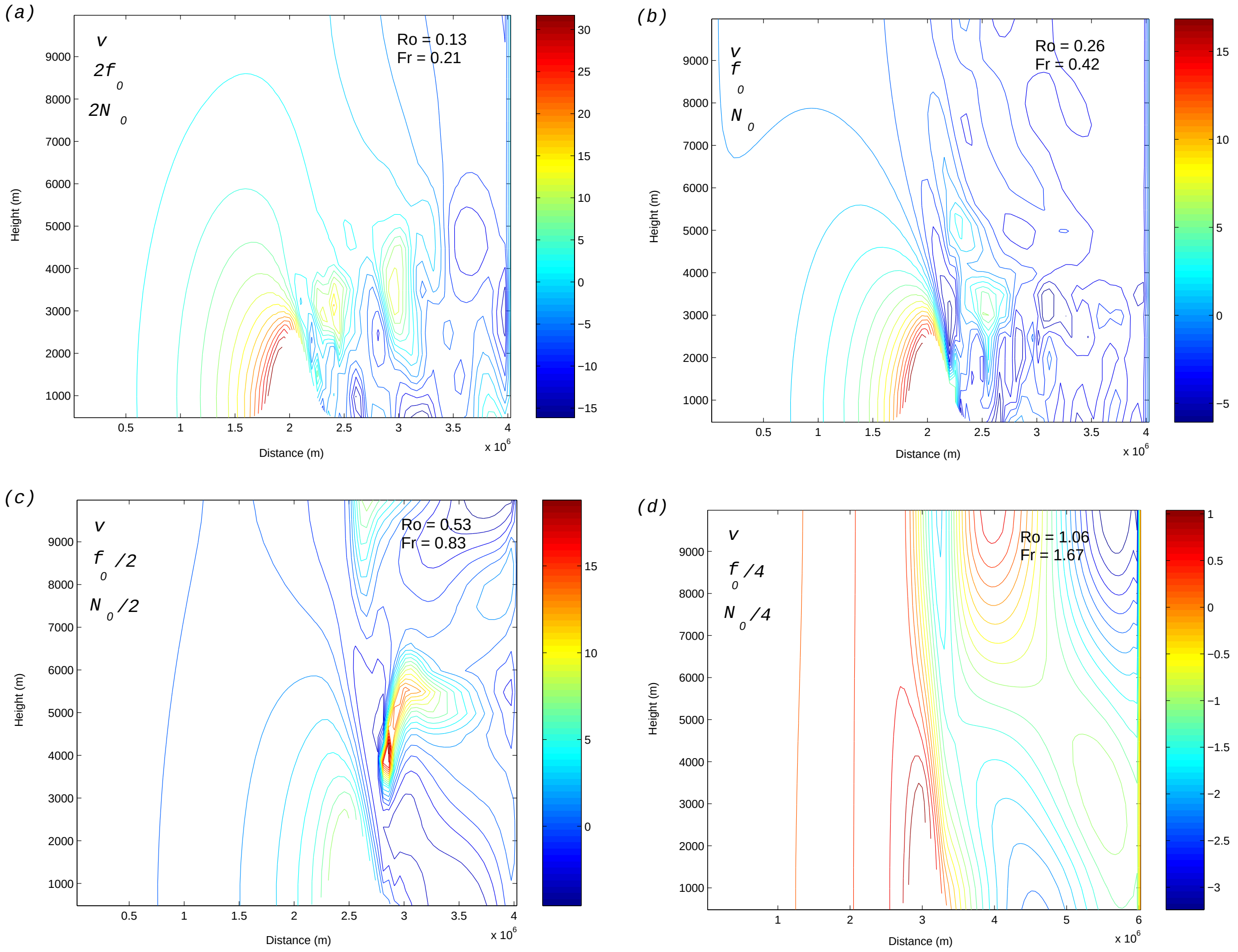

Figure 6.2: *Steady state* v *fields for (a)* $2f_0, 2N_0$*, (b)* f_0, N_0*, (c)* $f_0/2, N_0/2$ *and (d)* $f_0/4, N_0/4$*. Contour values are in accordance with the colour bar in* ms^{-1}*.*

From Fig. 6.3 we see an excellent linear relationship between the factor by which f and N are scaled and the maximum value of v in the barrier jet. Note that the point at the origin has been included because we know from Section 4.1 that when $f = 0$ the v field is zero everywhere. The line of best fit through the points is given by the equation

$$v_{max} = 17.8S_{f,N} - 0.903$$

where $S_{f,N}$ is the scaling factor.

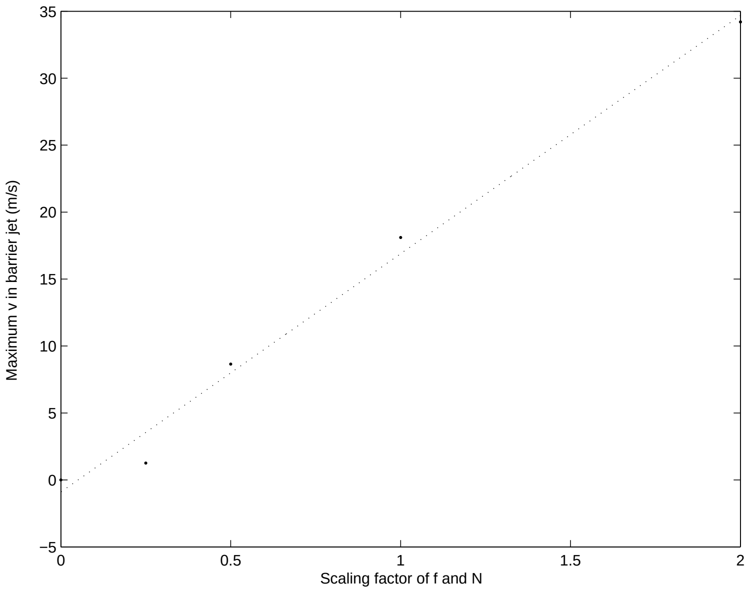

Figure 6.3: *Variation of v_{max} with scaling factor. The equation of the line of best fit is $v_{max} = 17.8S_{f,N} - 0.903$.*

Therefore, we could conclude that f/N is a useful parameter for determining the strength of the barrier jet.

6.2 Effect on vertical kinetic energy

As we have already seen from Section 4.3 that the effect of increasing Ro without any change in N is an increase in vertical kinetic energy. Here, we are also varying N and so Fr becomes an important parameter. We have already argued in Section 5.1 that with increasing Fr the vertical KE also increases. Therefore as we increase N we expect the vertical KE to decrease.

Figures 6.4 and 6.5 show the θ and w fields for the experiments in this chapter. Note that we have rearranged the panels so that Fig. 6.4(a)-(c) can easily be compared to Fig. 5.1(a)-(c) respectively. The solution in Fig. 6.4(d) does not reproduce the same Ro and Fr as any of the experiments in Chapter 5 and so will not be used for comparison.

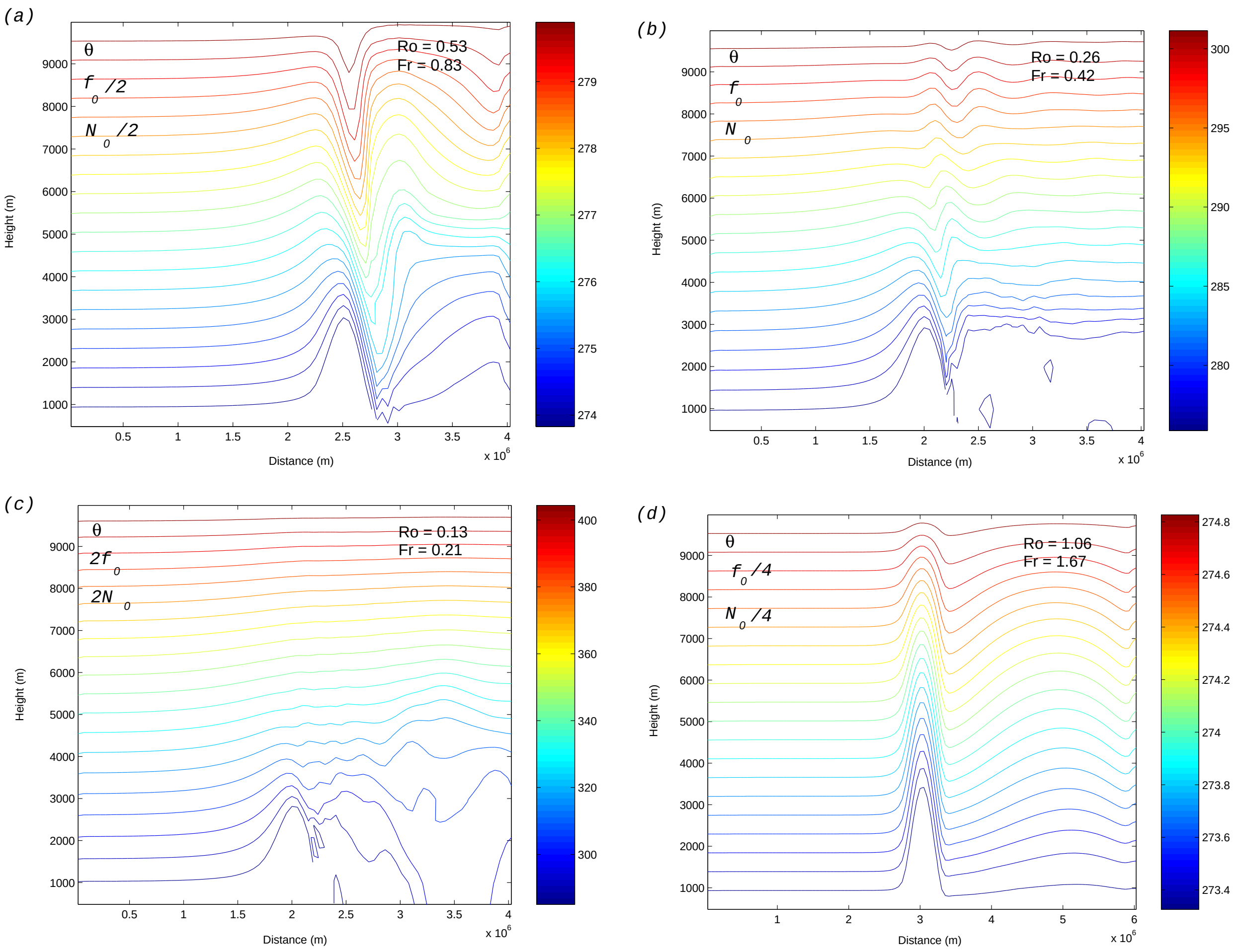

Figure 6.4: *Steady state θ fields for (a) $f_0/2, N_0/2$, (b) f_0, N_0, (c) $2f_0, 2N_0$ and (d) $f_0/4, N_0/4$. Contour values are in accordance with the colour bar in K.*

We expect solutions with the same Ro and Fr to be the same even though different variables may have been changed. Fig. 6.4(a) compares well with Fig. 5.1(a). The differences between the solutions downstream can be attributed to the right-hand boundary being closer to the mountain in Fig. 6.4(a) than Fig. 5.1(a). Figure 6.4(b) compares very well with Fig. 5.1(b). We suggest that these solutions in panels (a) and (b) are linear. When this is the case, Ro and Fr determine the solution well. Figure 6.4(c) is similar to Fig. 5.1(c) but does not agree completely. We suggest that this solution is nonlinear in which Ro and Fr do not determine the solution as well.

We can see from Figs. 6.4(a)-(c) that as Ro and Fr decrease the gravity wave activity

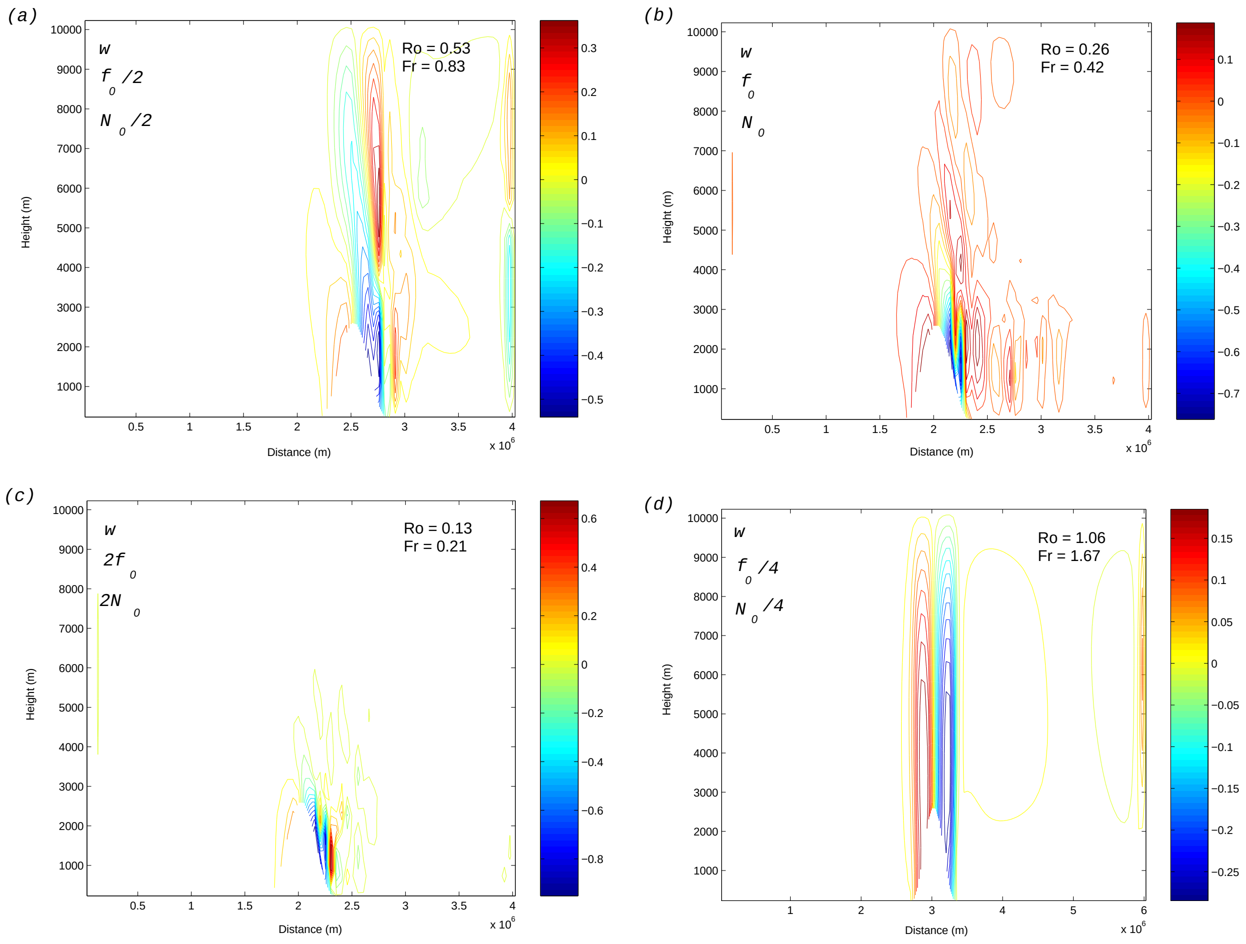

Figure 6.5: *Steady state* w *fields for (a)* $f_0/2, N_0/2$*, (b)* f_0, N_0*, (c)* $2f_0, 2N_0$ *and (d)* $f_0/4, N_0/4$*. Contour values are in accordance with the colour bar in* ms^{-1}*.*

appears to decrease. The vertical velocity fields (Figs. 6.5(a)-(c)) also show this decrease in vertical activity. However, in the $f_0/4, N_0/4$ case (Figs. 6.4(d) and 6.5(d)) $Fr > 1$ and $Ro > 1$. There are displacements centred over the mountain with amplitude that seems to decrease with height, followed by longer wavelength disturbances downstream of the mountain. The majority of the vertical motion occurs symmetrically over the mountain with upward motion upstream of the mountain throughout the height of the domain, and similarly downward motion downstream of the mountain (Fig. 6.5(d)). These vertical velocities are comparably weaker than in the previous cases.

Figure 6.6 shows the variation of the vertical kinetic energy with the scaling factor $S_{f,N}$. There is a clear increase of energy as the the scaling factor decreases, i.e. as f and N decrease (Fr and Ro increase), to a factor of 1/2. However, for $S_{f,N} = 1/4$ the vertical

KE is still substantial but less than for the $S_{f,N} = 1/2$ case. This could again be due to the apparent reduction in gravity wave activity as discussed above.

The scaling factors 2, 1 and 0.5 correspond to $Ro = 0.13$, 0.26 and 0.53 respectively. The trend of the vertical kinetic energy between these points compare swell to the points corresponding to $U = 5$, 10 and 20 in Fig. 5.3. We expect this to be the case.

We could conclude that f/N is a useful parameter for investigating gravity wave activity.

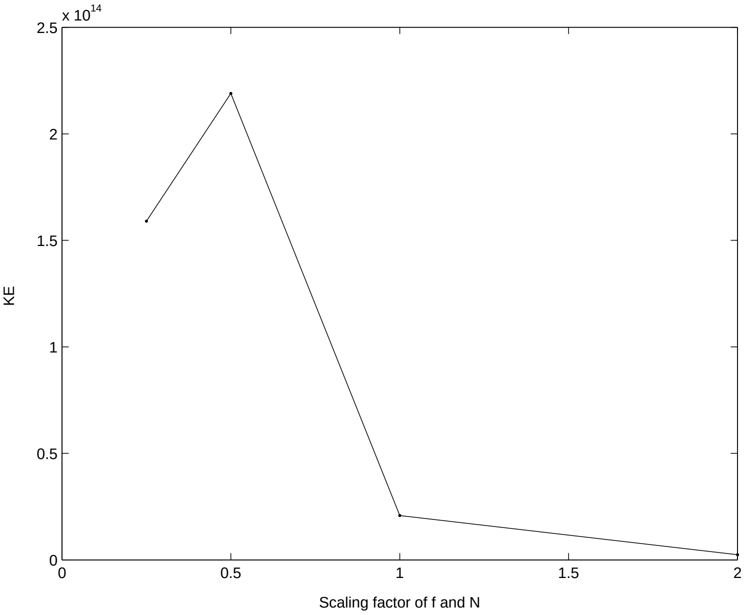

Figure 6.6: *Variation of vertical kinetic energy with scaling factor.*

6.3 Effect on pressure drag across the mountain

Figure 6.7 shows how the pressure drag across the mountain varies with the scaling factor of f and N. The drag does not vary by more than 20% from the mean value of the four points. Thus we could argue that by scaling f and N by the same factor and keeping f/N constant, the pressure drag remains unaffected.

The points corresponding to $S_{f,N} = 1$ and 0.5 agree extremely well with the points corresponding to $U = 10$ and 20 in Fig. 5.5. The point for $S_{f,N} = 2$ does not compare so well with $U = 5$.

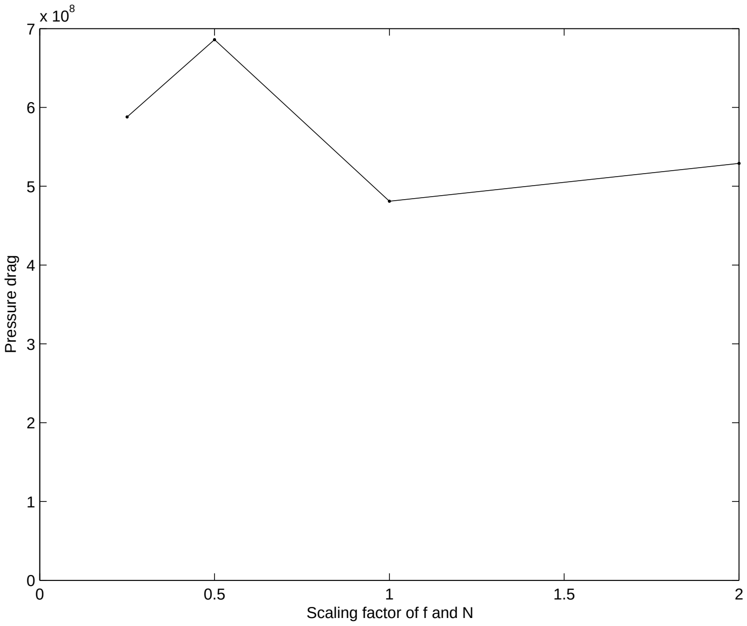

Figure 6.7: *Variation of the pressure drag across the mountain with scaling factor.*

Chapter 7

Discussion

A vertical slice version of the Met Office Unified model has been used to investigate the flow over an isolated cosine mountain. The stratification, N, and upstream flow speed, U, are both constant with height. The project aimed to simulate some of the features of flows over orography by varying just three dimensionless parameters. These were the Froude number ($Fr = U/NH$), Rossby number ($Ro = U/fL$) and ratio (f/N).

One of the main results of the project is that the limit $f \to 0$ is singular, i.e. the v fields of the flow solution did not converge towards the $f = 0$ solution. It also has multiple solutions; one for $f = 0$ and two obtained in the limits $f \to 0^+$ and $f \to 0^-$.

A well defined barrier jet exists even for small value of f because, from the horizontal momentum equation, a weak pressure gradient will still exist. As both f and N are scaled up the strength of the barrier jet increases linearly with the scaling factor. This suggests that the dimensionless parameter f/N is useful for determining the strength of the barrier jet. The barrier jet exists within the distance of upstream influence. The distance $\delta x = v_{max}/f$ agrees well with the theoretical Rossby radius of deformation, L_R, as f varies but the model upstream distance, L_m, differs substantially from both of these.

Vertical kinetic energy is used as a measure of gravity wave activity above the mountain. The amplitude of these waves increases as f decreases, however, for the $f = 0$ case the wave activity is less than for the $f = f_0/4$ case. Thus, we see that the vertical kinetic energy increases as f decreases apart from when $f = 0$ when it is much less than when

$f = f_0/4$. As f and N are both scaled down the gravity wave activity increases. In the case of decreased N, vertical displacements with increased amplitude become more possible. When $f = f_0/4$ and $N = N_0/4$, Ro and Fr exceed 1 and gravity wave activity appears to lessen. Therefore, vertical kinetic energy increases as the scaling factor decreases, apart from when the factor becomes less than 1/2 when the energy begins to decrease.

By decreasing U with all other parameters held constant, Ro and Fr are decreased at the same rate. As Ro decreases wave activity decreases and the solution gets closer to the semi-geostrophic solution. Convergence to this solution is second-order, as shown by the power law relationship between $\sqrt{KE}$ and U.

A drag on the mountain occurs when there is a pressure difference across it. As f decreases, the pressure drag increases in agreement with Smith (1979b). However, the drag for the $f = 0$ case is less than is less than that for the other f values. In the experiments where just U decreases so does the drag, though this is only a weak dependence. An interesting result is obtained when f and N are decreased together. Here, the pressure drag does not vary from the mean value by more than 20%. Therefore, we conclude that the pressure drag is unaffected by the scaling of f and N.

We expected solutions with the same Ro and Fr to be the same. The solutions in Chapter 6 for $Ro = 0.53$ and 0.26 agreed well with the corresponding solutions of Chapter 5 and we concluded these solutions were linear. The solutions for $Ro = 0.13$ agreed less well and we concluded this solution was nonlinear.

There are many other experiments that could have been conducted to further this project. An interesting one would have been to have two mountains with the distance between them being varied. Gap flows such as those discussed by Sprenger and Schär (2001) would occur as the upstream influence distance of the second mountain interfered with the lee side of the first mountain. Other experiments could have included changing the shape of the orography, and maybe varying its height.

References

Baines, P. G. 1987 Upstream blocking and airflow over mountains. *Ann. Rev. Fluid Mech.*, **19**, 75-97

Cullen, M. J. P., Chynoweth, S. and Purser, R. J. 1987 On semi-geostrophic flow over synoptic-scale topography. *Q. J. R. Meteorol. Soc.*, **113**, 163-180

Cullen, M. J. P., Davies, T., Mawson, M. H., James, J. A. and Coulter, S. 1997 An overview of numerical methods for the next generation U.K. NWP and climate model. Pp. 425-444 in *Numerical methods in atmosphere and ocean modelling, The Andre Robert Memorial Volume.* Eds. C. Lin, R. Laprise and H. Ritchie, Canadian Meteorological and Oceanographic Society, Ottawa, Canada

Cullen, M. J, P. 2000 On the accuracy of the semi-geostrophic approximation. *Q. J. R. Meteorol. Soc.*, **126**, 1099-1115

Cushman-Roisin, B. 1994 *Introduction to geophysical fluid dynamics.* Prentice Hall, New Jersey

Holton, J. R. 1992 *An introduction to dynamic meteorology.* Academic Press, London

McIlveen, R. 1997 *Fundamentals of weather and climate.* Chapman and Hall, London

Ólafsson, H. and Bougeault, P. 1997 The effect of rotation and surface friction on orographic drag. *J. Atmos. Sci.*, **54**, 193-210

Pierrehumbert, R. T. and Wyman, B. 1985 Upstream effects of mesoscale mountains. *J. Atmos. Sci.*, **42**, 977-1003

Quaile, E. L. 2001 Föhn and chinook winds. *Weather*, **56**, 141-145

Shutts, G. 1998 Idealised models of the pressure force on mesoscale mountain ridges. *Contrib. Atmos. Phys.*, **71**, 303-313

Smith, R. B. 1979a The influence of mountains on the atmosphere. *Adv. Geophys.*, **21**, 87-230

Smith, R. B. 1979b The influence of the earth's rotation on mountain wave drag. *J. Atmos. Sci.*, **36**, 177-180

Smith, R. B. 1989 Hydrostatic airflow over mountains. *Adv. Geophys.*, **31**, 1-41

Sprenger, M. and Schär, C. 2001 Rotational aspects of stratified gap flows and shallow föhn. *Q. J. R. Meteorol. Soc.*, **127**, 161-187

Acknowledgements

I would like to thank Professor Mike Cullen for his advice and guidance throughout the duration of this project and also thanks to Dr Pete Sweby and Sue Davis for all their assistance over the past year. Thanks are also due to my family who encouraged me that it was the right thing to do the course.

Thanks to Andy for helping me get rid of stress during many juggling sessions. Huge thanks go to Sal, for all her support and encouragement.

I also thank NERC for their financial support.

Declaration

'I confirm that this is my own work and the use of all material from other sources has been properly and fully acknowledged.'